

Response to the comments of Anonymous Referee #1

Li et al. present the evaluation of a custom ECCC-OFR design by performing characterization studies that included measurements of size-dependent particle transmission efficiency and yields of SOA generated from OH oxidation of α -pinene and C7, C10, and C12 n-alkanes in the presence and absence of ammonium sulfate seeds. Results are compared to those obtained with other OFRs and environmental chambers. Unlike in previous OFR studies, alkane-generated SOA did not exhibit a decrease in yield at high OH exposure due to fragmentation reactions. The ECCC-OFR is then used to investigate the SOA formation potential following OH oxidation of materials obtained from oil sands operations in Alberta. Cyclic alkanes are implicated as the most important class of precursors in the oil sands samples. Overall, the manuscript reads well. Given the emergence of OFRs as a technique to characterize SOA formation, and the application of the ECCC-OFR to study the aging of environmentally-relevant VOC mixtures that are emitted during oil sands extraction activities, I would support eventual publication of this manuscript in ACP. However, in its current form, I have reservations about assumptions that are made regarding laminar flow behavior, reduced wall losses compared to other OFRs, and SOA yield calculations that are heavily reliant on offline measurements of SOA precursor concentrations. In my opinion these assumptions are not adequately justified based on the current information that is given, and any related conclusions made about ECCC-OFR performance compared to other OFRs are uncertain at present.

Response: We thank Anonymous Referee #1 for the review and the positive evaluation of our manuscript. We have fully considered the comments, responded to these comments below in blue text and made the associated revisions to the manuscript as shown in red text. The response and changes are listed below.

General Comments

1. Recent OFR applications and modeling studies have demonstrated the utility of 185 nm radiation in OFRs due to ease of use in the field and due to additional HO_x generation via $\text{H}_2\text{O} + \text{h}\nu(185) \rightarrow \text{H} + \text{OH}$, $\text{H} + \text{O}_2 \rightarrow \text{HO}_2$. Here, the authors specifically mention that they chose to use mercury lamps that exclude the 185 nm emission line. Please explain the reasons for this choice.

Response: The lamps are located outside of the fused quartz reactor, and the transmittance of 185 nm UV light through fused quartz is very small, which limits the application of 185 nm UV lamps in our OFR. We calculate that only ~5% of the 185 nm light can be transmitted through the fused quartz wall; hence, 185 nm lamps were not used. Placing the lamps on the inside of the OFR to avoid this problem would have introduced additional surface areas and turbulence, thus negating some of the other advantages of this OFR, such as reduced wall losses. In addition, interior 185 nm lights would have made temperature control difficult. Exterior lamps allow the temperature of the OFR to be maintained accurately.

To address these points we added the following text in the revised manuscript (P4, L18-23):

“Recent OFR applications and modeling studies have demonstrated the utility of 185 nm radiation in OFRs due to ease of use in the field and due to additional OH and HO₂ generation (Li et al., 2015; Palm et al., 2016). However, the fused quartz tubes of ECCC-OFR limit the application of such lamps due to the low transmittance of 185 nm radiation (~5%), and placement of lamps on the interior of the OFR are likely to increase turbulence and wall losses within the OFR, and limit overall OFR temperature control. Consequently, 254 nm radiation lamps were used.”

2. The actinic flux at 254 nm is an important OFR characteristic that, unless I missed it, was never measured or calculated. It would be worthwhile to calculate this value and compare to the other OFR designs that are mentioned. For example, a possibility that is never discussed is whether potential SOA photolysis at 254 nm (which is more potentially important at high UV intensity and OH exposure) might be less important in the ECCC-OFR than in the PAM OFR due to lower actinic flux. I am not necessarily convinced that this is the case, but it should be briefly discussed and ruled out if not applicable. The preferable method to quantify the actinic flux would be to photolyze a compound with known absorption cross section at 254 nm as a function of lamp voltage. At the least, I think the maximum actinic flux inside the ECCC-OFR could be estimated from the wattage of the UV lamps at full output normalized by the internal surface area, with the caveat that I am not to what extent the mirrored enclosure referred to on P4, L14-15 would influence this calculation.

Response: We have now determined the maximum photon flux (with 4 lamps on) based upon the measured ozone decay and OH exposure (without precursor injection) combined with a photochemical box model characterizing radical chemistry in OFRs (Oxidation Flow Reactor Exposure Estimator 3.1) (Li et al., 2015; Peng et al., 2018). The input photon flux of the model was adjusted to match the measured ozone decay and OH exposure, which resulted in a maximum photon flux estimate of $\sim 1.9 \times 10^{16}$ photons $\text{cm}^{-2} \text{s}^{-1}$. This photon flux is similar to the PEAR OFR (2.3×10^{16} photons $\text{cm}^{-2} \text{s}^{-1}$) using the same estimation method (Ihalainen et al., 2019), and about three times that reported for the PAM (6.4×10^{15} photons $\text{cm}^{-2} \text{s}^{-1}$) (Lambe et al., 2017). Consequently, we can rule out the possibility of lower SOA photolysis in the ECCC-OFR as the reason for the higher yields in the ECCC-OFR compared to the PAM OFR.

The above content has been added to the revised manuscript (P4, L23-29).

3. In the ECCC-OFR, the authors state that an inlet with a cone angle of 30° is used to “minimize the establishment of jetting and recirculation in the OFR”, which is steeper than the 15° cone angle used by Huang et al. (2017) and the 14° cone angle used by Ihalainen et al. (2019). Whereas both of those studies employed CFD simulations to optimize their OFR design, there are no corresponding simulations of the ECCC-OFR fluid dynamics that support the 30° cone angle used here. Please provide supporting calculations and/or residence time distribution measurements supporting the claim that laminar flow is achieved and jetting/recirculation is not present when using a 30° cone angle.

Response: The reviewer is not comparing the same angles in the above comment. The cone angle mentioned in our paper (i.e., 30°) and Huang et al. (2017) is the full cone angle, while Ihalainen et al. (2019) reported the half cone angle. If the same angles are compared, then the half cone angles for the various OFRs are: 7.5° for Huang et al. (2017), 14° for Ihalainen et al. (2019), and 15° for the ECCC-OFR of this study. Hence, the cone angle of ECCC-OFR is very similar to that of the PEAR OFR (Ihalainen et al., 2019). This cone angle comparison was added to Sect. S1 of the Supplement.

To assess the near laminar flow of the ECCC-OFR, computational fluid dynamics (CFD) simulations were performed using ANSYS Fluent software (Version 2019 R2) in three dimensions to characterize the flow field inside the ECCC-OFR. Hybrid tetrahedral–hexahedral mesh consisting of 5.7×10^5 computation cells were used. Turbulence was modeled using a realizable k-epsilon model. The simulation results are shown in Fig. S4. It is shown in Fig. S4a that the flow velocity distribution in the reactor is generally uniform. A high velocity is observed only near the inlet, but reduces to the average velocity in

the conical diffuser. The velocity distribution here indicates that jetting is much weaker in ECCC-OFR compared to PAM (Mitroo et al., 2018). Fig. S4b indicates that the flow field is quite good in ECCC-OFR, with a small recirculation zone, similar to previous studies using a conical diffusion inlet (Huang et al., 2017; Ihalainen et al., 2019), but much better than PAM (Mitroo et al., 2018). **These CFD simulations were added to Sect. S2 of the Supplement.**

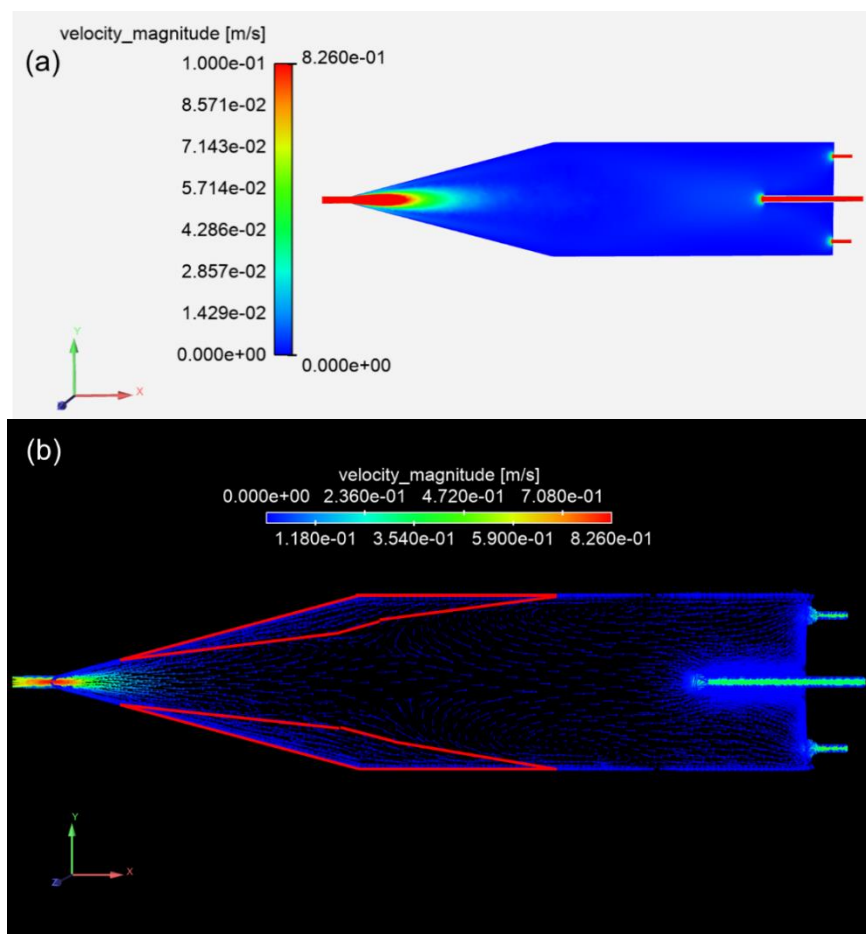


Figure S4. CFD simulation results: (a) velocity distribution; (b) vectors showing flow field. The red lines in (b) indicate the areas with recirculation.

4. The authors hypothesize that wall interactions are minor in the ECCC-OFR based on a calculation of the diffusion timescale (1400 sec) that is much longer than the residence time (120 sec) (P7, L1-8). Applying the same calculation to the PAM OFR, which has an inner radius of 10.2 cm, yields a diffusion timescale of 1474 sec. Given similar residence times and diffusion timescales, this line of reasoning would suggest similar wall interactions between the two systems. However, large-scale dispersion and recirculation inside OFRs (e.g. Lambe et al., 2011; Huang et al., 2017) complicates this sort of simple diffusion-based calculation. Later on (P9, L6-7), the authors speculate that higher SOA yields and less fragmentation are observed in the ECCC-OFR because of reduced wall interactions compared to other OFRs. This might be the case, but it is not supported by the logic presented above. This conclusion should be supported with a corresponding residence time distribution measurement and comparison to the RTD expected for ideal laminar flow, which was not performed here (P7, L9). In my opinion this is a critical

oversight that should be addressed. Additionally, I suggest measuring the yield of sulfuric acid generated from OH oxidation of SO₂ and comparing the result to other OFRs. Because sulfuric acid is not affected by photolysis or fragmentation, any difference in sulfuric acid yields between OFRs should be directly related to wall losses/interactions.

Response: Based upon the CFD simulation results above, we know that the flow field in ECCC-OFR is not perfectly ideal laminar flow, though it is significantly better than previous OFRs with a straight inlet, e.g., PAM (Mitroo et al., 2018). Hence, our assumption based on ideal laminar flow (using a diffusion timescale compared to the residence time to infer the gas-wall interactions) was removed in our revised paper (P7, L16-26).

The residence time distribution (RTD) was measured for ECCC-OFR and compared to ideal laminar flow in Fig. S5. The RTD was characterized by injecting a constant flow rate of CO₂ (10 s) into the OFR. The CO₂ concentration was then monitored from the sampling outlet of OFR with a CO₂ analyzer (Li-Cor LI-840A). The RTD was calculated from the differential CO₂ as a function of time elapsed since the start of injection. Fig. S5 indicates that the residence time associated with the CO₂ maximum intensity for the measured RTD and the ideal laminar flow RTD are in good agreement, and improved over the PAM and TPOT (Lambe et al., 2011). The shape of measured RTD before ~100 s is similar to the ideal laminar flow RTD, but slightly wider, which is likely due to dispersion. After ~100 s, the measured decrease in CO₂ is slower than for ideal laminar flow, which is likely due to recirculation in the OFR (Fig. S4).

This paragraph and associated figure were added to Sect. S2 of the Supplement.

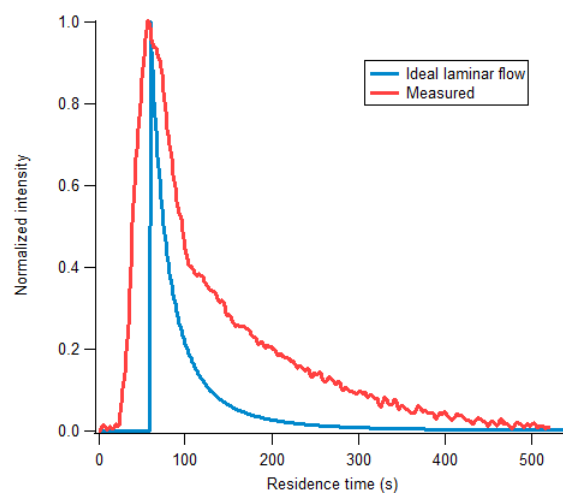


Figure S5. Residence time distribution (RTD) of CO₂ in ECCC-OFR compared to ideal laminar flow.

As suggested by the reviewer, the OH oxidation of SO₂ was performed in the ECCC-OFR. The SO₂ concentrations used were in the range of 24-63 ppb and the OH exposure was in the range of 3-10 × 10¹¹ molec cm⁻³ s, which are similar to those used in a previous PAM study (Lambe et al., 2011). The yield of sulfuric acid ($Y_{H_2SO_4}$) was calculated using the mass fraction of H₂SO₄ in particles ($x_{H_2SO_4}$), the SMPS-measured particle volume ($V_{H_2SO_4 \cdot H_2O}$, nm³ cm⁻³), the density of the particles ($\rho_{H_2SO_4 \cdot H_2O}$, g cm⁻³), and the measurement of the reacted SO₂ (ΔSO_2 , ppb), using an approach which has been described in detail previously (Lambe et al., 2011):

$$Y_{H_2SO_4} = \frac{x_{H_2SO_4} \times V_{H_2SO_4 \cdot H_2O} \times \rho_{H_2SO_4 \cdot H_2O}}{3.95 \times \Delta SO_2}$$

The $x_{H_2SO_4}$ and $\rho_{H_2SO_4 \cdot H_2O}$ were estimated using the Extended Aerosol Inorganic Thermodynamic Model (E-AIM) I (<http://www.aim.env.uea.ac.uk/aim/aim.php>) (Carslaw et al., 1995). The dry yield of H_2SO_4 from OH oxidation of SO_2 is $3.95 \mu\text{g m}^{-3}$ per ppb SO_2 reacted (Lambe et al., 2011); hence $Y_{H_2SO_4}$ is expected to be 100% without wall losses. As shown in Fig. S6, the yield of sulfuric acid is $100 \pm 4\%$ in this study, which is in agreement with the expected yield. The yield here is significantly higher than that obtained in previous OFR study using similar SO_2 concentrations and OH exposures (PAM and TPOT), which are mainly in the range of $\sim 15\%$ - 50% (Lambe et al., 2011). This may be a result of lower wall losses in current OFR for gas-phase sulfuric acid and/or particles. Given that sulfuric acid is not impacted by photolysis or fragmentation, the result here suggest that wall losses/interactions within the ECCC-OFR are significantly lower than previous OFRs that utilize straight inlets (PAM and TPOT).

The above paragraph was added to the revised manuscript (P7, L27-33; P8, L1-3) and the Supplement (Sect. S5).

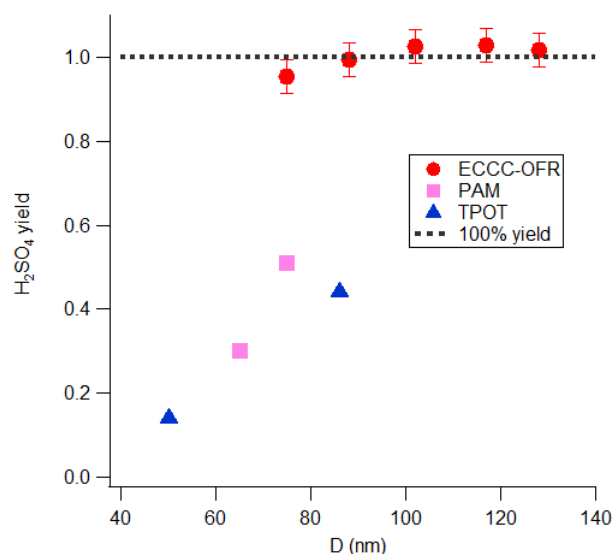


Figure S6. H_2SO_4 yields as a function of particle diameter in the ECCC-OFR and previous OFRs (Lambe et al., 2011).

Specific/Technical Comments

5. **P4, L16:** Please specify the O_3 mixing ratio (or range of O_3 mixing ratios) that was added to the OFR in these studies.

Response: The O_3 mixing ratio was ~ 12 ppm (now noted on P4, L17).

6. **P5, L5-7:** Because precursor concentrations were only obtained in offline measurements, how did the authors determine that the precursor concentrations remained constant and precise during the OFR experiments? As written, in the absence of other supporting/independent measurements this seems to be a major assumption and potential source of uncertainty in the SOA yield calculations.

Response: The THC concentration was measured before and after each experiment, and the difference was found to be less than 5%, representing a small uncertainty in the experiments. In addition, the precursor concentration was qualitatively checked during each experiment by repeating the same UV light intensity several times. For example, the UV lamp voltages were stepped from 120→50→60→120→70→80→120 etc... The absolute amount of SOA formed at the repeated light intensities varied by less than 5%, indicating that the THC precursor concentration was rather stable during experiments.

We have added the following text in the revised manuscript (P5, L22-24): “The THC concentration was measured before and after each experiment, resulting in differences of less than 5%. In addition, the magnitude of SOA formed for repeated experiments at the same light intensity varied by less than 5%, further indicating the stability of the precursor concentration over time.”

7. **Figure 1 and Section 3.1.1.**: The Lambe et al. 2011 reference used a Pyrex chamber, where wall losses of charged particles are higher than chambers made of conductive materials due to charge buildup on nonconductive surfaces. A better reference/comparison here would be to use the data from Figure S1 of Karjaranen et al. (2016) which used an aluminum chamber with conductive coating. Their particle transmission data is shown below for reference. Please modify the discussion and figure accordingly.

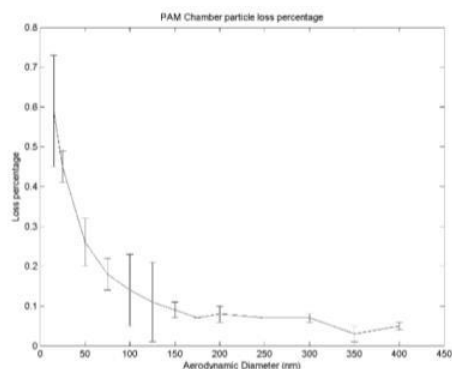


Figure S1. Primary particle losses in a similar PAM chamber that was used in the study.

Response: Particle transmission efficiencies from Karjalainen et al. (2016) and Ihalainen et al. (2019) were added in Figure 1 (now Figure 2).

The corresponding discussion was changed in the revised manuscript (P6, L28-31; P7, L1-2):

“The P_{trans} of other OFRs are also shown in Fig. 2 for comparison and indicates that the current P_{trans} is similar to that of the TSAR (TUT Secondary Aerosol Reactor) (Simonen et al., 2017) and PEAR (Ihalainen et al., 2019), likely due to the similarity in design (i.e., cone shaped inlet and sampling from the center-line, see Sect. S1 in Supplement). Conversely, the P_{trans} of the TPOT (Toronto Photo-Oxidation Tube), PAM-glass (PAM reactor with glass wall) (Lambe et al., 2011), PAM-metal (PAM reactor with metal wall) (Karjalainen et al., 2016), and CPOT (Caltech Photooxidation Flow Tube) (Huang et al., 2017) are 15-85%, 20-60%, 10-25%, and 20-45% lower respectively than the ECCC-OFR across a range of particle sizes.”

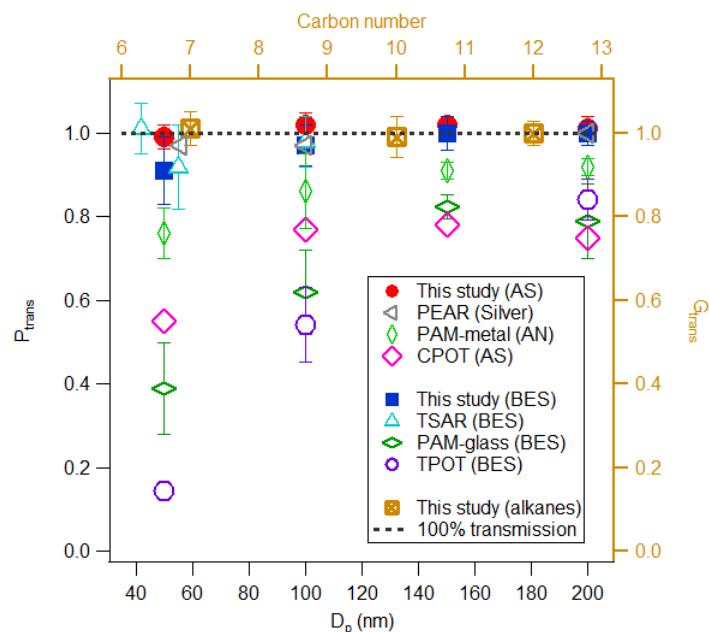


Figure 2. Particle (left and bottom axis) and gas (right and top axis) transmission efficiencies (P_{trans} and G_{trans}) for the ECCC-OFR. Particle transmission efficiencies of other OFRs are shown for comparison: PAM-glass and TPOT (Lambe et al., 2011), PAM-metal (Karjalainen et al., 2016), TSAR (Simonen et al., 2017), CPOT (Huang et al., 2017) and PEAR (Ihalainen et al., 2019).

8. **P15, L7:** The authors state: “all future OFR experiments should be conducted with seed particles to obtain more relevant qualitative and quantitative data.” I suggest making this statement in the specific context of laboratory SOA yield studies, as not all OFR experiments are intended to measure SOA yields and because addition of seed particles in ambient OFR experiments is not necessarily always desirable or practical.

Response: The line in has been revised as: “This suggests that future laboratory OFR experiments studying SOA yields should be conducted with seed particles to obtain more relevant qualitative and quantitative data.” (P15, L23-24).

9. **P11, L30 and Figure 4c:** Lambe et al. (2012) do not report absolute SOA yields from OH oxidation of diesel fuel and crude oil so it is unclear where this statement originates from.

Response: The carbon and oxygen yields of diesel fuel and crude oil in Figure 4c (now is Figure 5b) are what are referred to as the “normalized yields”. We do not use the absolute yields here as we only compare the relative change of yields (relative to the maximum yield) among different precursors.

We changed the figure caption to reflect this: “...normalized Y_C and Y_O for diesel and crude oil...” (P24, L6).

10. **Figure 1:** It may be worth adding particle transmission data from Ihalainen et al. (2019) to this figure. Also, how much passivation time is required to obtain 100% transmission efficiency of C7, C10 and C12 alkanes, and at what mixing ratios are they introduced to the ECCC-OFR?

Response: Particle transmission data from Ihalainen et al. (2019) are now added to Figure 1 (now Figure 2), see above response to Comment 7 for details.

The passivation time was 5-10 min, and the mixing ratio was 300-500 ppb for these alkanes (now noted in P7, L10-11).

11. **Figure 3:** I think this could be moved to the Supplement.

Response: This figure provides important information about the LVOC fates in ECCC-OFR, and can help to better understand the final corrected SOA yields from OS precursors. Hence, we have decided to keep it in the main manuscript.

12. **Figures 4-6 and related text:** I suggest a reorganization to improve clarity and flow. First, move the current Figure 5 to the Supplement or to Methods. Second, combine the current Figure 6a with the current Figures 4a and 4b into a single 3-panel figure. Third, move the current Figure 4d into a separate figure and place between current Figures 4 and 6.

Response: Figure 5 is now Figure 1 and is described in Methods (P5, L27-28): “The chromatogram and the derived VD of the OS-related precursors are shown in Fig. S2 and Fig. 1 and discussed in detail in Sect. S4 of the Supplement.”

Figures 1-3 are now Figures 2-4; Figure 6a is now moved into Figure 5 as Figure 5d; Figure 4d is now Figure 6; Figure 6b is now Figure 7.

The corresponding text is revised to match the Figure numbers above.

References

- Carslaw, K. S., Clegg, S. L., and Brimblecombe, P.: A Thermodynamic Model of the System HCl-HNO₃-H₂SO₄-H₂O, Including Solubilities of HBr, from <200 to 328 K, *The Journal of Physical Chemistry*, 99, 11557-11574, 10.1021/j100029a039, 1995.
- Huang, Y., Coggon, M. M., Zhao, R., Lignell, H., Bauer, M. U., Flagan, R. C., and Seinfeld, J. H.: The Caltech Photooxidation Flow Tube reactor: design, fluid dynamics and characterization, *Atmospheric Measurement Techniques*, 10, 839-867, 10.5194/amt-10-839-2017, 2017.
- Ihalainen, M., Tiitta, P., Czech, H., Yli-Pirilä, P., Hartikainen, A., Kortelainen, M., Tissari, J., Stengel, B., Sklorz, M., Suhonen, H., Lamberg, H., Leskinen, A., Kiendler-Scharr, A., Harndorf, H., Zimmermann, R., Jokiniemi, J., and Sippula, O.: A novel high-volume Photochemical Emission Aging flow tube Reactor (PEAR), *Aerosol Science and Technology*, 53, 276-294, 10.1080/02786826.2018.1559918, 2019.
- Karjalainen, P., Timonen, H., Saukko, E., Kuuluvainen, H., Saarikoski, S., Aakko-Saksa, P., Murtonen, T., Bloss, M., Dal Maso, M., Simonen, P., Ahlberg, E., Svenningsson, B., Brune, W. H., Hillamo, R., Keskinen, J., and Rönkkö, T.: Time-resolved characterization of primary particle emissions and secondary particle formation from a modern gasoline passenger car, *Atmospheric Chemistry and Physics*, 16, 8559-8570, 10.5194/acp-16-8559-2016, 2016.
- Lambe, A., Massoli, P., Zhang, X., Canagaratna, M., Nowak, J., Daube, C., Yan, C., Nie, W., Onasch, T., Jayne, J., Kolb, C., Davidovits, P., Worsnop, D., and Brune, W.: Controlled nitric oxide production via O(¹S) + N₂O reactions for use in oxidation

- flow reactor studies, *Atmospheric Measurement Techniques*, 10, 2283-2298, 10.5194/amt-10-2283-2017, 2017.
- Lambe, A. T., Ahern, A. T., Williams, L. R., Slowik, J. G., Wong, J. P. S., Abbatt, J. P. D., Brune, W. H., Ng, N. L., Wright, J. P., Croasdale, D. R., Worsnop, D. R., Davidovits, P., and Onasch, T. B.: Characterization of aerosol photooxidation flow reactors: heterogeneous oxidation, secondary organic aerosol formation and cloud condensation nuclei activity measurements, *Atmospheric Measurement Techniques*, 4, 445-461, 10.5194/amt-4-445-2011, 2011.
- Li, R., Palm, B. B., Ortega, A. M., Hlywiak, J., Hu, W., Peng, Z., Day, D. A., Knote, C., Brune, W. H., de Gouw, J. A., and Jimenez, J. L.: Modeling the radical chemistry in an oxidation flow reactor: radical formation and recycling, sensitivities, and the OH exposure estimation equation, *The journal of physical chemistry. A*, 119, 4418-4432, 10.1021/jp509534k, 2015.
- Mitroo, D., Sun, Y., Combet, D. P., Kumar, P., and Williams, B. J.: Assessing the degree of plug flow in oxidation flow reactors (OFRs): a study on a potential aerosol mass (PAM) reactor, *Atmospheric Measurement Techniques*, 11, 1741-1756, 10.5194/amt-11-1741-2018, 2018.
- Palm, B. B., Campuzano-Jost, P., Ortega, A. M., Day, D. A., Kaser, L., Jud, W., Karl, T., Hansel, A., Hunter, J. F., Cross, E. S., Kroll, J. H., Peng, Z., Brune, W. H., and Jimenez, J. L.: In situ secondary organic aerosol formation from ambient pine forest air using an oxidation flow reactor, *Atmospheric Chemistry and Physics*, 16, 2943-2970, 10.5194/acp-16-2943-2016, 2016.
- Peng, Z., Palm, B. B., Day, D. A., Talukdar, R. K., Hu, W., Lambe, A. T., Brune, W. H., and Jimenez, J. L.: Model Evaluation of New Techniques for Maintaining High-NO Conditions in Oxidation Flow Reactors for the Study of OH-Initiated Atmospheric Chemistry, *ACS Earth and Space Chemistry*, 2, 72-86, 10.1021/acsearthspacechem.7b00070, 2018.
- Simonen, P., Saukko, E., Karjalainen, P., Timonen, H., Bloss, M., Aakko-Saksa, P., Rönkkö, T., Keskinen, J., and Dal Maso, M.: A new oxidation flow reactor for measuring secondary aerosol formation of rapidly changing emission sources, *Atmospheric Measurement Techniques*, 10, 1519-1537, 10.5194/amt-10-1519-2017, 2017.

Response to the comments of Anonymous Referee #2

Summary:

The oil sands (OS) in Alberta, Canada provide a significant source of SOA, necessitating lab studies to isolate contributions from different sources and chemical reactions. To address this knowledge gap, the authors use a custom oxidative flow reactor (OFR) to mimic different degrees of atmospheric oxidative aging for emissions from different OS-related precursors. In this work, the authors introduce the ECCC-OFR through single-species precursor experiments to assess the impacts of gas and particle wall losses and seeding, then use the ECCC-OFR to evaluate differences in OS-related SOA formation between several relevant sources. This is generally a clearly written manuscript, with compelling results that contribute important knowledge for both OS SOA chemistry as well as future OFR laboratory studies.

Response: We thank Anonymous Referee #2 for the review and the positive evaluation of our manuscript. We have fully considered the comments and made the associated revisions to our manuscript. The responses (blue text) and changes to the manuscript (red text) are listed below.

General Comments

[1] In the introduction (page 2, lines 22-24), the authors state that organic gases from the OS are mainly alkanes that react with the OH radical. However, one of the precursors that the authors use and discuss in the introduction is α -pinene. The choice of α -pinene is confusing in this context without further justification. From the manuscript, it seems that α -pinene was chosen because it was convenient to compare OFR operation to other studies. Does α -pinene have additional relevance for SOA in the OS region? Either way, it would be helpful for the author to address this choice early on in the manuscript. Additionally, under the ECCC-OFR operating conditions for these experiments (i.e., precursor concentrations, ozone concentrations), is there potential for the interfering α -pinene + ozone reaction to contribute significantly to SOA yields?

Response: According to our previous study (Liggio et al., 2016), α -pinene is likely the main SOA precursor for background OA in the OS region. We have added the following content in the revised manuscript for clarity (P3, L18-20): “Alkanes are the main component of OS emissions, while α -pinene is a representative biogenic precursor which likely contributes significantly to the background SOA observed in OS region (Liggio et al., 2016).”

We have also added “Under the operating conditions used here for α -pinene experiments, OH reaction contributes 64%-98% of the α -pinene gaseous loss across the entire OH exposure range, and >90% after 3 equivalent days, with α -pinene + O₃ reaction playing a minor role” in P8, L8-10 of the revised manuscript.

[2] Wall losses (Section 3.1.1): The authors state that vapor wall losses are likely minimal based on the diffusion timescale relative to the residence time within the reactor, then state the critical assumption that flow in the reactor is ideally laminar. Is this assumption solely based on fluid dynamics information from previously designed OFRs? The authors cite CFD done by Huang et al. (2017) for the CPOT on page 4 (lines 6-7) to justify the assumption, but I'm curious as to how the differences between the ECCC-OFR and the CPOT would change the fluid dynamics. For example, the ECCC-OFR has a straight outlet rather than a conical one like the CPOT. Is there potential for jetting or dead volume around the outlet? What are the benefits to sampling from the center line?

Response: We have now performed CFD simulations on the ECCC-OFR and included these results in the Supplement (Sect. S2).

To assess the near laminar flow of the ECCC-OFR, computational fluid dynamics (CFD) simulations were performed using ANSYS Fluent software (Version 2019 R2) in three dimensions to characterize the flow field inside the ECCC-OFR. Hybrid tetrahedral–hexahedral mesh consisting of 5.7×10^5 computation cells were used. Turbulence was modeled using a realizable k-epsilon model. The simulation results are shown in Fig. S4. It is shown in Fig. S4a that the flow velocity distribution in the reactor is generally uniform. A high velocity is observed only near the inlet, but reduces to the average velocity in the conical diffuser. The velocity distribution here indicates that jetting is much weaker in ECCC-OFR compared to PAM (Mitroo et al., 2018). Fig. S4b indicates that the flow field is quite good in ECCC-OFR, with a small recirculation zone, similar to previous studies using a conical diffusion inlet (Huang et al., 2017; Ihalainen et al., 2019), but much better than PAM (Mitroo et al., 2018).

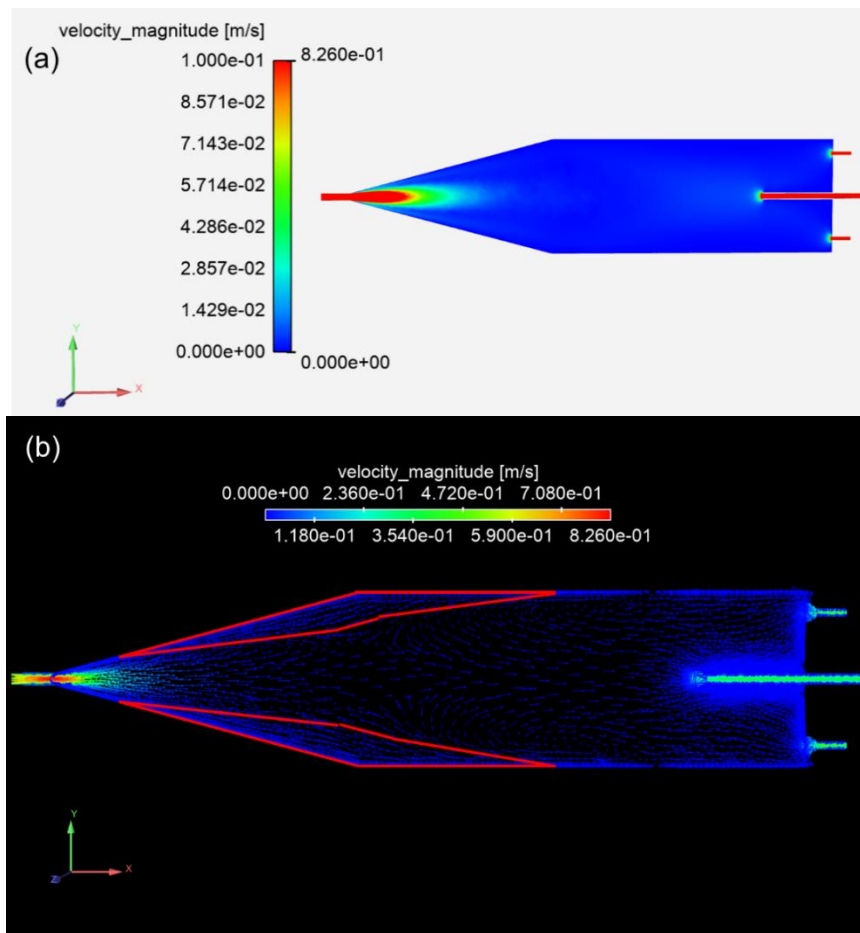


Figure S4. CFD simulation results: (a) velocity distribution; (b) vectors showing flow field. The red lines in (b) indicate the areas with recirculation.

Based upon the CFD simulation results above, we know that the flow field in ECCC-OFR is not perfectly ideal laminar flow, though it is significantly better than previous OFRs with a straight inlet, e.g., PAM (Mitroo et al., 2018). Hence, our assumption based on ideal laminar flow (using a diffusion timescale

compared to the residence time to infer the gas-wall interactions) was removed in our revised paper (P7, L16-26).

From the CFD simulation results above, we also know that there is no jetting or dead volume around the sampling outlet. The non-laminar flow at the end of the OFR only influences the side flow, not the sampling flow.

The benefits to sampling from the centerline is the minimization of the interactions with walls (Lambe et al., 2011), as most of the flow that interacts with the walls exit from the side outlets.

Technical Comments

[1] Page 2, Lines 19-20: The authors state that a single species approach to studying SOA formation is “impractical.” To me, “impractical” implies some sort of logistical difficulty and sells the point short. I’d consider reframing this sentence to emphasize atmospheric relevance for the OS, which is critical to consider when performing lab studies.

Response: We changed the sentence into “As a result, using a single species approach to studying SOA formation from OS is unrepresentative.” (P2, L19-20).

[2] Page 2, Lines 21-22: Consider restructuring this sentence for clarity. Perhaps “Precursor emissions occur throughout the OS surface mining and processing production cycle, and they originate from sources including...”

Response: This sentence was modified to be “Precursor emissions occur throughout the OS surface mining and processing production cycle, and they originate from sources including open pit surface mines, processing plants and tailings ponds” (P2, L21-22).

[3] Page 2, Line 24: Define “OH” as “hydroxyl radicals (OH)” before using the abbreviation.

Response: Revised (P2, L24).

[4] Page 2, Line 28: “Complimentary” should be “complementary.” This spelling should also be changed on page 3, line 13.

Response: Revised (P2, L28; P3, L13).

[5] Page 3, Line 6: Replace the semicolon after “vary” with a comma.

Response: Revised (P3, L6).

[6] Page 4, Line 11: Replace “Hg” with “mercury.”

Response: Revised (P4, L12).

[7] Page 5, Line 5: Define the THC acronym here.

Response: Revised (P5, L17).

[8] Figure 1: Consider matching the color of the top and right axes to the alkane data points to visually distinguish the gas-phase data from the particle-phase data.

Response: The Figure 1 (now is Figure 2) is revised to be:

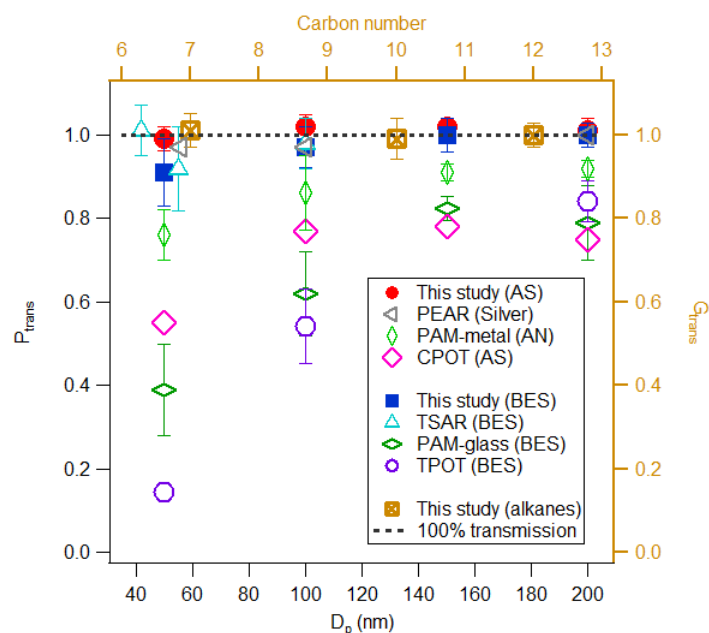


Figure 2. Particle (left and bottom axis) and gas (right and top axis) transmission efficiencies (P_{trans} and G_{trans}) for the ECCC-OFR. Particle transmission efficiencies of other OFRs are shown for comparison: PAM-glass and TPOT (Lambe et al., 2011), PAM-metal (Karjalainen et al., 2016), TSAR (Simonen et al., 2017), CPOT (Huang et al., 2017) and PEAR (Ihalainen et al., 2019).

[9] Page 8, line 9: The sentence starting with “This despite” is not a full sentence.

Response: This sentence was merged with previous sentence to be “...for unseeded experiments, despite initial concentrations of...” (P9, L5).

[10] Page 10, line 21: Replace the semicolon after “mixtures” with a comma.

Response: Revised (P11, L9).

[11] Page 10, line 25: It would be helpful to cite the specific section in supporting information so the reader can easily flip to it as needed.

Response: It was modified to be “... as described in detail in Sect. S5 of the Supplement” (P11, L13).

[12] Figure 4a and 4b: Consider emphasizing the different y axis scales between the two panels in either the text or the figure caption. Otherwise, the differences between seeded and non-seeded results can be difficult to pick out visually.

Response: “Note that the y-axis ranges are different in (a), (c), and (d)” was added in the figure caption (P24, L8).

[13] I would be interested to see the AMS mass spectra for each OS-related oxidation experiment, perhaps in the supplement.

Response: The AMS mass spectra for each OS-related oxidation experiment are shown in Figure S9. We have added “Although these precursors have very different SOA yields, their AMS mass spectra (Fig. S9) are similar, indicating a similar main precursor composition (alkanes)” at P11, L25-26 of the revised manuscript.

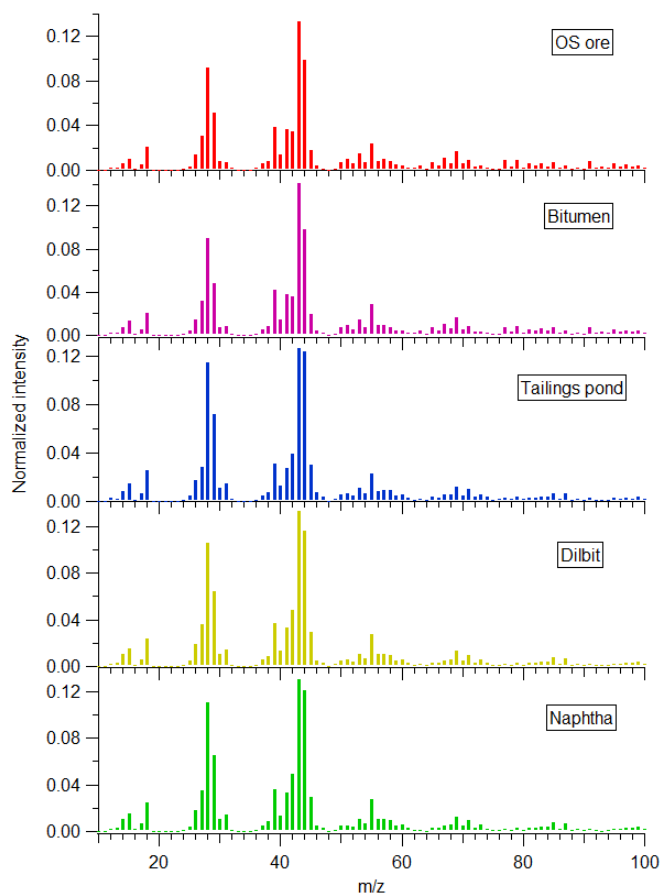


Figure S9. Representative AMS mass spectra for each OS-related oxidation experiment at OH exposure of $\sim 1.5 \times 10^{12}$ molec cm^{-3} s.

References

- Huang, Y., Coggon, M. M., Zhao, R., Lignell, H., Bauer, M. U., Flagan, R. C., and Seinfeld, J. H.: The Caltech Photooxidation Flow Tube reactor: design, fluid dynamics and characterization, *Atmospheric Measurement Techniques*, 10, 839-867, 10.5194/amt-10-839-2017, 2017.
- Ihalainen, M., Tiitta, P., Czech, H., Yli-Pirilä, P., Hartikainen, A., Kortelainen, M., Tissari, J., Stengel, B., Sklorz, M., Suhonen, H., Lamberg, H., Leskinen, A., Kiendler-Scharr, A., Harndorf, H., Zimmermann, R., Jokiniemi, J., and Sippula, O.: A novel high-volume Photochemical Emission

- Aging flow tube Reactor (PEAR), *Aerosol Science and Technology*, 53, 276-294, 10.1080/02786826.2018.1559918, 2019.
- Karjalainen, P., Timonen, H., Saukko, E., Kuuluvainen, H., Saarikoski, S., Aakko-Saksa, P., Murtonen, T., Bloss, M., Dal Maso, M., Simonen, P., Ahlberg, E., Svenningsson, B., Brune, W. H., Hillamo, R., Keskinen, J., and Rönkkö, T.: Time-resolved characterization of primary particle emissions and secondary particle formation from a modern gasoline passenger car, *Atmospheric Chemistry and Physics*, 16, 8559-8570, 10.5194/acp-16-8559-2016, 2016.
- Lambe, A. T., Ahern, A. T., Williams, L. R., Slowik, J. G., Wong, J. P. S., Abbatt, J. P. D., Brune, W. H., Ng, N. L., Wright, J. P., Croasdale, D. R., Worsnop, D. R., Davidovits, P., and Onasch, T. B.: Characterization of aerosol photooxidation flow reactors: heterogeneous oxidation, secondary organic aerosol formation and cloud condensation nuclei activity measurements, *Atmospheric Measurement Techniques*, 4, 445-461, 10.5194/amt-4-445-2011, 2011.
- Liggio, J., Li, S. M., Hayden, K., Taha, Y. M., Stroud, C., Darlington, A., Drollette, B. D., Gordon, M., Lee, P., Liu, P., Leithead, A., Moussa, S. G., Wang, D., O'Brien, J., Mittermeier, R. L., Brook, J. R., Lu, G., Staebler, R. M., Han, Y., Tokarek, T. W., Osthoff, H. D., Makar, P. A., Zhang, J., Plata, D. L., and Gentner, D. R.: Oil sands operations as a large source of secondary organic aerosols, *Nature*, 534, 91-94, 10.1038/nature17646, 2016.
- Mitroo, D., Sun, Y., Combest, D. P., Kumar, P., and Williams, B. J.: Assessing the degree of plug flow in oxidation flow reactors (OFRs): a study on a potential aerosol mass (PAM) reactor, *Atmospheric Measurement Techniques*, 11, 1741-1756, 10.5194/amt-11-1741-2018, 2018.
- Simonen, P., Saukko, E., Karjalainen, P., Timonen, H., Bloss, M., Aakko-Saksa, P., Rönkkö, T., Keskinen, J., and Dal Maso, M.: A new oxidation flow reactor for measuring secondary aerosol formation of rapidly changing emission sources, *Atmospheric Measurement Techniques*, 10, 1519-1537, 10.5194/amt-10-1519-2017, 2017.

Secondary organic aerosol formation from α -pinene, alkanes and oil sands related precursors in a new oxidation flow reactor

Kun Li, John Liggio, Patrick Lee, Chong Han, Qifan Liu, and Shao-Meng Li

Air Quality Research Division, Environment and Climate Change Canada, Toronto, Ontario M3H 5T4, Canada.

5 **Correspondence:** John Liggio (john.liggio@canada.ca)

Abstract. Oil sands (OS) operations in Alberta, Canada are a large source of secondary organic aerosol (SOA). However, the SOA formation process from OS-related precursors remains poorly understood. In this work, a newly developed oxidation flow reactor (OFR), the Environment and Climate Change Canada OFR (ECCC-OFR), was characterized and used to study the yields and composition of SOA formed from OH oxidation of α -pinene, selected alkanes, and the vapors evolved from five
10 OS-related samples (OS ore, naphtha, tailings pond water, bitumen, and dilbit). The derived SOA yields from α -pinene and selected alkanes using the ECCC-OFR were in good agreement with those of traditional smog chamber experiments, but significantly higher than those of other OFR studies under similar conditions. The results also suggest that gas-phase reactions leading to fragmentation (i.e., C-C bond cleavage) have a relatively small impact on the SOA yields in the ECCC-OFR at high photochemical ages, in contrast to other previously reported OFR results. Translating the impact of fragmentation reactions in
15 the ECCC-OFR to ambient atmospheric conditions reduces its impact on SOA formation even further. These results highlight the importance of careful evaluation of OFR data, particularly when using such data to provide empirical factors for the fragmentation process in models. Application of the ECCC-OFR to OS-related precursor mixtures, demonstrated that the SOA yields from OS ore and bitumen vapors (maximum of ~0.6-0.7) are significantly higher than those from the vapors from solvent use (naphtha), effluent from OS processing (tailing pond water) and from the solvent diluted bitumen (dilbit) (maximum of
20 ~0.2-0.3), likely due to the volatility of each precursor mixture. A comparison of the yields and elemental ratios (H/C and O/C) of the SOA from the OS-related precursors to those of linear and cyclic alkane precursors of similar carbon numbers suggests that cyclic alkanes play an important role in the SOA formation in the OS. The analysis further indicates that the majority of the SOA formed downwind of OS facilities is derived from open-pit mining operations (i.e., OS ore evaporative emissions), rather than from higher volatility precursors from solvent use during processing and/or tailing management. The current results
25 have implications for improving the regional modeling of SOA from OS sources, for the potential mitigation of OS precursor emissions responsible for observed SOA downwind of OS operations, and for the understanding of petrochemical and alkane derived SOA in general.

1 Introduction

Over the last several decades, oil production from unconventional sources has increased significantly and is expected to continue to increase into the future due to its abundant reserves, particularly in North America (Alboudwarej et al., 2006; Mohr and Evans, 2010; Owen et al., 2010). The Alberta oil sands (OS) is a large unconventional crude oil deposit, which is extracted through both open-pit mining and in-situ steam assisted techniques. Considering the scale of OS oil production, a number of environmental concerns associated with OS air emissions have arisen, including the potential for ecosystem toxicity (Kirk et al., 2014; Harner et al., 2018) and acid deposition (Jung et al., 2011; Makar et al., 2018). Recent field measurements have shown that OS mining and processing facilities are a large source of volatile organic compounds (VOCs) (Simpson et al., 2010; Li et al., 2017). Such gaseous air pollutants are rapidly transformed into secondary organic aerosol (SOA), for which the OS has been shown to be a large source (Liggio et al., 2016). Despite the large SOA formation rates observed in the OS (~45-84 ton day⁻¹) (Liggio et al., 2016), the emission sources, chemical compositions, volatilities and SOA forming potentials of the precursors remain unclear. Understanding the impact of SOA on the regional PM_{2.5} burden, air quality and potentially regional climate requires accurate model predictions of SOA, which have been limited by the lack of data on OS source specific SOA precursors and their SOA forming potential (Stroud et al., 2018).

Investigating SOA forming potentials of hydrocarbons is generally accomplished through targeted experiments of single precursor compounds of interest to derive a yield (Odum et al., 1996; Kroll and Seinfeld, 2008). However, in the OS, SOA precursors are highly complex mixtures with volatilities spanning the range of volatile organic compounds (VOC; saturation concentration $C^* > 3 \times 10^6 \mu\text{g m}^{-3}$) to semi-volatile organic compounds (SVOC; $C^* = 0.3 - 300 \mu\text{g m}^{-3}$) (Donahue et al., 2012; Liggio et al., 2016; Tokarek et al., 2018). As a result, using a single species approach to studying SOA formation from OS is unrepresentative. In addition, the mix of precursors (and hence chemical properties) varies by source within any given OS facility. Precursor emissions occur throughout the OS surface mining and processing production cycle, and they originate from sources including open pit surface mines, processing plants and tailings ponds. The organic gases evaporated from these OS sources are mainly alkanes of diverse structure (e.g., linear, branched and cyclic) (Simpson et al., 2010; Li et al., 2017), which primarily react with hydroxyl radicals (OH) in the atmosphere, as their reactions with NO₃ radical and O₃ are very slow (Atkinson and Arey, 2003). Consequently, the mixture of vapors evolved from the above sources are ideally suited to experimental studies of their overall SOA forming potentials/yields with oxidation flow reactors (OFRs) where ozone is often utilized as an OH radical precursor.

The development of OFRs has recently provided a complementary approach to traditional large volume smog chambers to investigate SOA formation processes (Kang et al., 2007; Lambe et al., 2011; Bruns et al., 2015). The advantages associated with the use of OFRs include their ability to probe the SOA forming potentials of a real-world mixture of precursors, and to study SOA formation on short time scales, simulating up to several weeks of OH radical exposure (Lambe et al., 2015; Bruns et al., 2015; Palm et al., 2016). OFRs have been utilized in numerous studies to investigate the SOA forming potentials of bulk gasoline and diesel emissions (Tkacik et al., 2014; Karjalainen et al., 2016; Jathar et al., 2017; Simonen et al., 2017), biomass

burning emissions (Ortega et al., 2013; Bruns et al., 2015), ambient air at numerous locations (Ortega et al., 2016; Palm et al., 2016) and single precursors (Kang et al., 2011; Lambe et al., 2011; Lambe et al., 2012; Lambe et al., 2015). The results of several OFR studies have also been used to infer the presence of gas-phase fragmentation reactions (i.e., C-C bond cleavage) (Jimenez et al., 2009), the transition between functionalization (i.e., oxygen addition) and fragmentation (Lambe et al., 2012), and the corresponding impact of these processes on SOA formation yields of single precursors and complex mixtures (Lambe et al., 2012; Tkacik et al., 2014). However, results from OFR studies vary, with some single precursor experiments noting significantly lower SOA yields from OFRs compared to smog chambers (e.g., isoprene and *m*-xylene) (Lambe et al., 2011; Lambe et al., 2015), and others indicating similar but consistently lower yields than traditional smog chamber results (e.g., α -pinene) (Bruns et al., 2015; Lambe et al., 2015). Additionally, studies of vehicle exhaust mixtures in OFRs generally exhibit reduced SOA potential relative to smog chambers at similar photochemical ages (Tkacik et al., 2014; Jathar et al., 2017; Simonen et al., 2017). Similarly, the impact of fragmentation on SOA yields in OFRs have been reported to be relatively large at moderate to high OH exposures in some studies (Lambe et al., 2012; Lambe et al., 2015) but negligible in others (Bruns et al., 2015). Although the use of OFRs has been suggested as a complementary approach to smog chambers, such disparities between OFR experiments, and between OFR and chamber results, is likely to make the interpretation of OFR SOA yields and their application to air quality modeling systems difficult. This is particularly relevant for the use of OFRs with a complex mixture of precursors.

In this study, the application of a newly developed OFR (the Environment and Climate Change Canada OFR, ECCC-OFR) to single compounds (alkanes and α -pinene) and complex precursor mixtures is described. Alkanes are the main component of OS emissions, while α -pinene is a representative biogenic precursor which likely contributes significantly to the background SOA observed in OS region (Liggio et al., 2016). The derived SOA yields for these single compounds are compared with those of other OFRs and smog chambers, providing improved confidence in the use of OFRs for the determination of SOA yields, and in the understanding of the relative importance of fragmentation processes to SOA formation. The ECCC-OFR is further used here to study the OH initiated formation of SOA from various OS derived complex mixtures under low-NO_x conditions. These mixtures are representative of the potential pollution from distinct stages of the OS production cycle and/or sources. This new information on the yields of SOA from these varied OS sources and other single compounds will improve the understanding of SOA formation from this large industrial sector, advance the modeling of the OS SOA formation in regional air quality models, and improve the overall understanding of alkane derived SOA in general.

2 Methods

SOA formation was investigated using a custom-made OFR (ECCC-OFR), which is shown schematically in Fig. S1. The design of the ECCC-OFR was partially based upon recent OFRs designs (Lambe et al., 2011; Huang et al., 2017; Simonen et al., 2017) with several specific differences described further in the Supplement (Sect. S1). Briefly, the reactor is a fused quartz cylinder with a cone shaped diffusion inlet. The length of the cylinder is 50.8 cm, with an inner diameter of 20.3 cm. The

length of the cone inlet is 35.6 cm, with a full cone angle of 30°. The conical inlet is designed to minimize the establishment of jetting and recirculation in the OFR (Huang et al., 2017), which were noted for straight OFR inlets (Huang et al., 2017; Mitroo et al., 2018). There are seven openings at the output end of the ECCC-OFR; six of them (I.D.=0.25”) are equally spaced around the perimeter to provide side flow as exhaust with a distance to the walls of 2.5 cm, intended to reduce the impact of gas and particle wall losses on sampling. A stainless steel sampling port (O.D.=0.25”, I.D.=0.18”) is located in the center of the reactor, protruding 12.7 cm into the ECCC-OFR to minimize the influence of any potential turbulent eddies induced at the end of the reactor. Computational fluid dynamics (CFD) simulations and residence time distribution (RTD) measurements were conducted for this OFR, and the results indicate that only a small area is affected by recirculation and a near laminar flow is likely achieved (Sect. S2 and Figs. S4 and S5 of the Supplement). The volume from the inlet of the cone to the sampling port is approximately 16 L. The total flow rate for experiments is 8 L min⁻¹, resulting in a residence time of 120 s. The sampling flow rate is approximately 1.6 L min⁻¹ (determined by the flow of instruments connected), with an additional flow (6.4 L min⁻¹) pushed out of the reactor through the side ports as exhaust. Four ozone-free mercury UV lamps (BHK Inc.) used to generate OH radical are located in four open-ended fused quartz tubes that are parallel and external to the OFR (1.5 cm). The lamps are purged by a large flow of air (~30 L min⁻¹) through the quartz tubes to remove the heat generated by lamps, resulting in a working temperature of approximately 25 °C, which is slightly higher than room temperature. The entire reactor is contained in an internally mirrored polycarbonate enclosure to direct all produced light towards the reactor.

OH radicals were generated by photolysis of O₃ (~12 ppm) at 254 nm followed by reaction with water vapor, a commonly used method in many OFRs (Kang et al., 2007; Lambe et al., 2012; Liu et al., 2014). Recent OFR applications and modelling studies have demonstrated the utility of 185 nm radiation in OFRs due to ease of use in the field and due to additional OH and HO₂ generation (Li et al., 2015; Palm et al., 2016). However, the fused quartz tubes of ECCC-OFR limit the application of such lamps due to the low transmittance of 185 nm radiation (~5%), and placement of lamps on the interior of the OFR are likely to increase turbulence and wall losses within the OFR, and limit overall OFR temperature control. Consequently, 254 nm radiation lamps were used. The maximum photon flux (with 4 lamps on) was determined based upon the measured ozone decay and OH exposure (without precursor injection) combined with a photochemical box model characterizing radical chemistry in OFRs (Oxidation Flow Reactor Exposure Estimator 3.1) (Li et al., 2015; Peng et al., 2018). The input photon flux of the model was adjusted to match the measured ozone decay and OH exposure, which resulted in a maximum photon flux estimate of ~1.9 × 10¹⁶ photons cm⁻² s⁻¹. This photon flux is similar to the PEAR OFR (2.3 × 10¹⁶ photons cm⁻² s⁻¹) using the same estimation method (Ihalainen et al., 2019), and about three times that reported for the PAM (6.4 × 10¹⁵ photons cm⁻² s⁻¹) (Lambe et al., 2017). The relative humidity was detected at the outlet (side flow) of the reactor with a humidity sensor (Vaisala), and was maintained at 37% ± 2% at room temperature (21 ± 1°C) by controlling the flow of dry and wet zero air into the reactor. The OH exposure (photochemical age) inside the reactor was estimated through the decay of CO due to its reaction with OH (Li et al., 2015). The CO was introduced into the ECCC-OFR during separate experiments to characterize OH exposure off-line. The CO concentration was measured with a CO analyzer (LGR CO-23r) with a high precision (0.1 ppb). A low initial concentration of CO (~0.5 ppm) was used to minimize the external OH reactivity introduced by CO, hence

increasing the accuracy of OH exposure estimation (Li et al., 2015). The OH radical concentration was adjusted through changes in the UV light intensity by varying the voltage applied to the lamps. The OH exposure during experiments ranged from $1.2 \times 10^{10} - 2.3 \times 10^{12}$ molec cm^{-3} s, which corresponds to 0.1 – 18 days of photochemical age, assuming a global average OH concentration of 1.5×10^6 molec cm^{-3} (Mao et al., 2009). However, the equivalent aging time is significantly shorter for urban areas and OS production regions, because of their typically higher ambient OH concentrations (Hofzumahaus et al., 2009; Stone et al., 2012). For example, the OH exposure range is equivalent to 20 min – 2.7 days if assuming an average OH concentration of 1×10^7 molecules cm^{-3} as has been estimated for the plumes originating from Alberta OS operations (Liggio et al., 2016).

Vapors from α -pinene, individual alkanes (*n*-heptane, *n*-decane, *n*-dodecane, cyclodecane and decalin) and various OS related samples (with the exception of the tailings pond sample) were introduced into the ECCC-OFR by a small flow of zero air ($0.5\text{-}2$ ml min^{-1}) passing over the headspace of the sample material, which was placed in a glass U-tube and maintained at room temperature. The OS samples included freshly mined OS ore (original, unprocessed), bitumen (processed heavy oil product), naphtha (a solvent used in OS processing), diluted bitumen (dilbit, a mixture of bitumen and solvent for transport in pipelines), and tailings pond water (waste water from the mining and processing) (see Sect. S3 in the Supplement for details). The tailings pond sample (~ 2 L) was placed into a 4 L glass bottle and was bubbled into the ECCC-OFR. For some samples with high volatilities (e.g., naphtha and *n*-heptane), the gas-phase was further diluted before being injected into the reactor. Total hydrocarbon (THC) concentration entering the ECCC-OFR was determined by passing the input gas stream (in off-line experiments) through a Pt based catalytic converter maintained at 400 °C and measuring the subsequently evolved CO_2 (Licor LI-840A) as described by Veres et al. (2010). The evolved CO_2 concentration (ppb) is converted to the total C concentration (ppbC, see Table 1). The conversion efficiency of this THC system was measured to be $100 \pm 2\%$ for several hydrocarbons in the range of $\text{C}_7\text{-C}_{18}$ (see Sect. S7 and Fig. S2 in the Supplement), but has been shown to be equally efficient at lower carbon numbers (Veres et al., 2010). The THC concentration was measured before and after each experiment, resulting in differences of less than 5%. In addition, the magnitude of SOA formed for repeated experiments at the same light intensity varied by less than 5%, further indicating the stability of the precursor concentration over time. For complex OS precursor mixtures introduced into the OFR, a volatility distribution (VD) was measured by collecting the vapor-phase onto desorption tubes containing Tenax (Gerstel) followed by analysis with a thermo-desorption gas chromatography–mass spectrometer (TD-GC-MS, Agilent) utilizing a method described previously (Liggio et al., 2016). The chromatogram and the derived VD of the OS-related precursors are shown in Fig. S3 and Fig. 1 and discussed in detail in Sect. S4 of the Supplement.

Particle size distributions at the exit of the OFR were measured with a scanning mobility particle sizer (SMPS, TSI), which were used to determine SOA yields. For a subset of experiments, ammonium sulfate (AS) seed particles were generated with an atomizer, dried with a diffusion dryer, and introduced into the reactor without size selecting. The mass concentration of the AS seed particles was approximately 20 $\mu\text{g m}^{-3}$ for most experiments with a number-weighted mode diameter of approximately 50 nm (mass-weighted mode diameter ~ 90 nm). For OS ore and naphtha, additional seed concentration experiments (~ 10 and 40 $\mu\text{g m}^{-3}$) were also performed to investigate the impact of seed concentration on SOA formation.

Particle composition was determined using a long time-of-flight aerosol mass spectrometer (LToF-AMS, Aerodyne) with a mass resolution of 6000-8000 in V-mode. The mass spectra and elemental properties of the SOA were determined using the AMS analysis software Squirrel (Version 1.57I) and Pika (Version 1.16I). The elemental ratios (H/C and O/C) were estimated using the improved ambient method described previously (Canagaratna et al., 2015). The SOA mass concentration was calculated by multiplying the integrated volume concentration from the SMPS (after subtracting the AS volume concentration for seeded experiments) by the effective particle density. The effective density (ρ , 1.35-1.6 for different precursors) was calculated from the vacuum aerodynamic diameter (D_{va} , obtained from the AMS) and the electric mobility diameter (D_m , obtained from the SMPS) for non-seeded experiments using the equation $\rho = D_{va} / D_m$ (Lambe et al., 2015). The same density was used for seeded and non-seeded experiments.

10 In the current study, only low- NO_x experiments were performed for all precursors, in which the reaction with HO_2 radical dominates the fate of the peroxy radical (RO_2) formed in the initial OH reaction. Such conditions are likely to represent the atmospherically relevant scenario where OS emissions have been transported significantly downwind of the OS region (and NO consumed), over boreal forest areas, where there were few NO_x sources. In addition, the low- NO_x condition is a typical oxidation pathway parameterized in regional air quality models. The formation of OS derived SOA under high- NO_x conditions (closer to sources) is the topic of a forthcoming publication.

3 Results and discussion

3.1 Characterization of the ECCC-OFR

3.1.1 Wall losses

Previous OFR studies have indicated that the wall losses of both gaseous precursors and formed particles are potentially important factors in influencing the SOA yield results from OFRs (Lambe et al., 2011; Lambe et al., 2015; Huang et al., 2017; Simonen et al., 2017). The particle wall losses for the ECCC-OFR were assessed by measuring size-selected (50 nm, 100 nm, 150 nm and 200 nm diameter) inorganic (ammonium sulfate, AS) (Huang et al., 2017) and organic (bis(2-ethylhexyl) sebacate, BES) (Lambe et al., 2011; Simonen et al., 2017) aerosol number concentrations before entering and after exiting the reactor. As shown in Fig. 2, the concentration of AS aerosols after the reactor is within $\pm 3\%$ of the concentration before the reactor. For BES, the particle transmission efficiency (P_{trans}) is 92% at 50 nm and increases to $\sim 100\%$ for 100 nm and larger particles. This indicates that inorganic and organic particle wall losses of the ECCC-OFR were very small for the flow conditions and particle size range in the experiments, and hence were not considered in further SOA yield calculations. The P_{trans} of other OFRs are also shown in Fig. 2 for comparison and indicates that the current P_{trans} is similar to that of the TSAR (TUT Secondary Aerosol Reactor) (Simonen et al., 2017) and PEAR (Ihalainen et al., 2019), likely due to the similarity in design (i.e., cone shaped inlet and sampling from the center-line, see Sect. S1 in the Supplement). Conversely, the P_{trans} of the TPOT (Toronto Photo-Oxidation Tube), PAM-glass (PAM reactor with glass wall) (Lambe et al., 2011), PAM-metal (PAM

reactor with metal wall) (Karjalainen et al., 2016), and CPOT (Caltech Photooxidation Flow Tube) (Huang et al., 2017) are 15-85%, 20-60%, 10-25%, and 20-45% lower respectively than the ECCC-OFR across a range of particle sizes. Potential causes of these discrepancies include recirculation and turbulence induced by a straight inlet and/or output sampling end (Lambe et al., 2011), non-centerline sampling (Huang et al., 2017) and longer residence times (Huang et al., 2017) in the other 5 OFRs (see Sect. S1 in the Supplement), which have been noted as potential factors previously (Lambe et al., 2011; Simonen et al., 2017; Mitroo et al., 2018).

The transmission efficiencies of the ECCC-OFR for gaseous hydrocarbons (G_{trans}) in the volatile to intermediate volatility ranges were also determined using the THC conversion methodology described above to measure the concentration immediately before entering and after exiting the reactor. The G_{trans} results for three *n*-alkanes, specifically *n*-heptane (C_7), *n*-decane (C_{10}) and *n*-dodecane (C_{12}) are shown in Fig. 2, and are approximately 100%±3%. The passivation time was 5-10 min, and the mixing ratio was 300-500 ppb for these alkanes. Measurement data with respect to hydrocarbon transmission efficiency for the other OFRs are not currently available for comparison. While the loss of hydrocarbon precursors in the ECCC-OFR may be minimal, one cannot easily measure the losses of lower volatility oxygenated compounds directly, particularly those of intermediate products of oxidation, which largely influence measured SOA yields in smog chambers and the other OFRs 15 (Zhang et al., 2014; Palm et al., 2016). Alternatively, we use the secondary formation of sulfuric acid to evaluate the wall losses of gas-phase products, which is described below. ~~However, an approximate indication of the potential for gaseous wall losses is provided by estimating the characteristic time associated with diffusion from the center to walls of the ECCC OFR as described previously (Huang et al., 2017). The characteristic diffusion time (τ_e) in the radial direction is given by~~

$$\tau_e = \frac{R^2}{D_i}, \quad (1)$$

20 ~~where R is the inner radius of the ECCC OFR, and D_i is the molecular diffusivity of species i in air (Huang et al., 2017). A typical estimate of the molecular diffusivity for oxidized organic vapor (with a molecular weight of 200 g mol⁻¹) in air is $\sim 7 \times 10^{-6}$ m² s⁻¹ (Tang et al., 2015; Palm et al., 2016), leading to a τ_e of ~ 1400 s. This characteristic diffusion time is much longer than the average residence time in the reactor (120 s), suggesting that the interaction of gases at the ECCC OFR center with the walls is likely very small. As a result, we suggest that the wall losses for intermediate oxygenated products on the measured 25 SOA yields were minor, although this would in part also depend on the ideality of laminar flow at the sampling point of the ECCC OFR which was not assessed.~~

The OH oxidation of SO₂ was performed in the ECCC-OFR. The SO₂ concentrations used were in the range of 24-63 ppb and the OH exposure was in the range of 3-10 × 10¹¹ molec cm⁻³ s, which are similar to those used in a previous PAM study (Lambe et al., 2011). The yield of sulfuric acid was calculated using a method described previously (Lambe et al., 2011), 30 and is shown in detail in Sect. S5 of the Supplement. As shown in Fig. S6, the yield of sulfuric acid is 100±4% in this study, which is in agreement with the expected yield (Sect. S5 of the Supplement). The yield here is significantly higher than that obtained in previous OFR study using similar SO₂ concentrations and OH exposures (PAM and TPOT), which are mainly in the range of ~15%-50% (Lambe et al., 2011). This may be a result of lower wall losses in current OFR for gas-phase sulfuric

acid and/or particles. Given that sulfuric acid is not impacted by photolysis or fragmentation, the result here suggest that wall losses/interactions within the ECCC-OFR are significantly lower than previous OFRs that utilize straight inlets (PAM and TPOT).

3.1.2 SOA yields and fragmentation

5 An important performance characteristic of an OFR is the ability to derive SOA yields consistent with previous results in traditional chamber experiments (Bruns et al., 2015;Lambe et al., 2015). The SOA yields from the ECCC-OFR (under low-NO_x conditions), for selected individual compounds (α -pinene, *n*-decane (C₁₀), *n*-dodecane (C₁₂)), as a function of photochemical age or OH exposure and in the presence or absence of AS seed aerosol are provided in Fig. 3. Under the operating conditions used here for α -pinene experiments, OH reaction contributes 64%-98% of the α -pinene gaseous loss across the entire OH exposure range, and >90% after 3 equivalent days, with α -pinene + O₃ reaction playing a minor role. The SOA yields (Y) in Fig. 3 are calculated using the mass concentration of organic aerosols (ΔM_O) and reacted parent hydrocarbons (ΔHC , see Sect. S5 in the Supplement for details), where $Y = \Delta M_O / \Delta HC$. Figure 3 also shows the yields from other recent smog chamber and OFR studies for the same individual precursors under low-NO_x conditions (see Table 2 for details) (Ng et al., 2007;Eddingsaas et al., 2012;Lambe et al., 2012;Chen et al., 2013;Loza et al., 2014;Lambe et al., 2015;Bruns et al., 2015;Han et al., 2016).

As most previous smog chamber studies are carried out at relatively low OH exposures, limited data can be used for comparison, since the majority of chamber data resides in the photochemical age less than 3 equivalent days (3.9×10^{11} molecules OH cm⁻³ s⁻¹, Table 2). However, in addition to the OH exposure level, numerous other factors may affect the SOA yield comparisons between OFR and chambers. These factors include the concentration of gas phase precursor utilized, the presence or absence of seed aerosol, and the mass of SOA formed during experiments (Odum et al., 1996;Donahue et al., 2006;Kroll et al., 2007;Kroll and Seinfeld, 2008;Hallquist et al., 2009). Nonetheless, the α -pinene SOA yields in the ECCC-OFR are similar to previous chamber experiments at similar OH exposures (Fig. 3a, Table 2). Given the known dependence of yield on SOA mass and precursor concentration (Odum et al., 1996;Kroll and Seinfeld, 2008), slightly higher yields for α -pinene are expected from chamber studies (and observed), as some experiments were performed at SOA mass levels and gaseous precursor concentrations 3-14 and 3-15 times (Ng et al., 2007;Eddingsaas et al., 2012;Bruns et al., 2015) greater than the current study (22-42 $\mu\text{g m}^{-3}$ and 13.7 ppb; see Table 2 for details). Considering the impact of these conditions on yields, the ECCC-OFR SOA yields of α -pinene are in reasonable agreement with those derived from chamber studies. However, in the case of alkanes, the agreement is significantly different. While the initial *n*-dodecane concentration and OA concentration (upper limit) in a previous study (Loza et al., 2014) were ~3 times higher than this study (Table 2), the corresponding SOA yields were significantly lower (Fig. 3b) than the current results. The known impact of gaseous wall losses on SOA yields in environmental chambers (Zhang et al., 2014) suggests the long residence time of those particular experiments (~36 hours) (Loza et al., 2014) likely resulted in significant intermediate gaseous product wall losses and correspondingly low SOA yields compared to the ECCC-OFR (which has minimal wall losses).

While the SOA yields for single precursors from the present study are in reasonable agreement with traditional chamber data, they are significantly larger than those of other OFR data sets (Lambe et al., 2012;Chen et al., 2013;Lambe et al., 2015;Bruns et al., 2015) (Figs. 3a and b). With the exception of the lowest OH exposure data point for α -pinene oxidation, the SOA yields quickly diverge from each other after approximately 2 equivalent photochemical days (a factor of 4 larger in this study after ~ 10 equivalent days) for unseeded experiments, despite initial concentrations of α -pinene (41-100 ppb) and SOA mass ($90 \mu\text{g m}^{-3}$) in previous OFR experiments (Chen et al., 2013;Lambe et al., 2015) being considerably higher than the current study (13.3 ppb and $37.9 \mu\text{g m}^{-3}$) at similar photochemical ages (Table 2). For seeded experiments of α -pinene, the current SOA yields are higher than those reported by Bruns et al. (2015), despite their precursor concentration and SOA mass being 10-25 and 5-24 times higher than this study (13.7 ppb and $41.9 \mu\text{g m}^{-3}$, Table 2). Similarly, the present SOA yields for *n*-decane (C_{10}) diverge from previously reported results (Lambe et al., 2012) (Fig. 3b), with the present SOA yields up to a factor of 4 higher after ~ 10 equivalent photochemical days ($1.3 \times 10^{12} \text{ molecules cm}^{-3} \text{ s OH exposure}$). It is noteworthy that the yields for *n*-decane from the present study and reported by Lambe et al. (2012) are in reasonable agreement for up to 2 equivalent days ($2.6 \times 10^{11} \text{ molecules cm}^{-3} \text{ s OH exposure}$). However, this is likely fortuitous, as the SOA mass concentration and precursor concentration in the study by Lambe et al. (2012) ($231 \mu\text{g m}^{-3}$ and 102 ppb) was an order of magnitude higher than in the present study ($30.4 \mu\text{g m}^{-3}$ and 23.4 ppb , Table 2), which will enhance the gas-particle partitioning process and lead to higher yields. Such an effect has been observed in C_{15} SOA experiments (Lambe et al., 2012), where decreasing the aerosol mass concentration from $100 \mu\text{g m}^{-3}$ to $16 \mu\text{g m}^{-3}$ reduced the SOA yield from 0.69 to 0.21.

The decrease in yield at longer photochemical ages (higher OH exposures) in previous OFR studies (Figs. 3a and b) has been attributed to gas-phase fragmentation leading to higher volatility SOA products, with a transition point between functionalization and fragmentation observed at the maximum carbon yield (Lambe et al., 2012). The SOA carbon and oxygen yields (Y_C and Y_O) for α -pinene and *n*-decane from the current experiments are shown in Fig. 3c following the approach outlined elsewhere (Kroll et al., 2009;Lambe et al., 2012) and presented in details in the Supplement (Sect. S5). In the absence of gaseous wall losses, the impact of fragmentation may be indicated by a relatively larger decrease in Y_C at higher OH exposure compared to Y_O (Kroll et al., 2009;Lambe et al., 2012). Such an effect is observed in the present results for both α -pinene and *n*-decane (Fig. 3c), with Y_C decreasing by 38% and 15% over 7 and 13 photochemical days, respectively. The maximum Y_O is at a higher photochemical age compared to Y_C for SOA formed from both precursors (~ 9 and 4 photochemical days for α -pinene; ~ 13 and 6 photochemical days for *n*-decane), further consistent with a transition from functionalization to fragmentation in these experiments as indicated in Fig. 3c. However, the relative impact of fragmentation on the overall SOA yields here is in contrast to that suggested previously (Lambe et al., 2012) (Figs. 3a and b). The maximum Y_C for *n*-decane here is observed at a higher photochemical age of 6 days, compared to 4 days seen by Lambe et al. (2012), and the decrease in Y_C and overall Y is also significantly less (15% vs $\sim 95\%$ for Y_C ; $<5\%$ vs $\sim 95\%$ for Y).

Given the similarity in the OH exposure range used between studies, and the generally higher SOA mass concentration (and precursor concentration) in previous OFR studies (Lambe et al., 2012;Chen et al., 2013;Lambe et al., 2015), the present results suggest that gaseous wall losses during the oxidation process may have reduced previously observed yields in their

OFRs, thereby leading to an overemphasis on the importance of fragmentation to SOA formation. It is notable that the relative impact of fragmentation here, although small, may also not be fully applicable to the ambient atmosphere due to the fate of low volatility organic compounds (LVOCs) in the OFRs. Accounting for the fate of LVOCs reduces the potential importance of fragmentation to SOA formation in this study and the ambient atmosphere even further, as is described below (Sect. 3.1.3).

5 3.1.3 Fate of LVOCs

Previous studies have demonstrated that SOA yields derived in OFRs at high OH exposures (and other conditions) have likely been underestimated, due to differences between the fates of LVOCs in OFRs and the ambient atmosphere (Palm et al., 2016). There are four possible fates associated with LVOCs in an OFR: condensation to aerosol, reaction with OH, condensation to the OFR walls, and exiting the OFR (then lost on sampling walls). However, in the ambient atmosphere, condensation to aerosol is the dominant fate of LVOCs, indicating that the other three possible fates are limitations of the OFR (Palm et al., 2016). To characterize the ECCC-OFR with respect to the fate of LVOC and improve the subsequent applicability of the data to the ambient atmosphere, we modeled the fate of LVOCs under conditions specific to these experiments, following the approach of Palm et al. (2016), as described further in the Supplement (Sect. S6).

The modeled fates of LVOCs in the ECCC-OFR for unseeded and AS seeded conditions are shown in Figs. 4a and b, using the parameters (OH concentration and aerosol size distribution) from α -pinene experiments. Figure 4a indicates that condensation on aerosol surfaces (in the absence of seed particles, for α -pinene derived SOA) accounts for 70%-80% of the LVOC fate between ~1-6 photochemical days, decreasing to 40%-50% at 16 photochemical days. These fractions are similar to an ambient OFR study conducted in Los Angeles (~40%-80%) (Ortega et al., 2016), but higher than that obtained at a forested site (~10%-70%) (Palm et al., 2016). OH oxidation accounts for 5%-50% of the LVOC loss in the ECCC-OFR, increasing in importance at higher photochemical age, while LVOC wall losses and OFR exiting fates are very small, generally less than 5%. For experiments using 20 $\mu\text{g m}^{-3}$ of AS seed particles, the fraction that condenses onto aerosol (~70-95%; Fig. 4b) is significantly higher than that for unseeded experiments, due to the presence of a higher condensational sink.

The fraction of LVOCs that condenses on aerosol (F_{aerosol}) for single precursors (α -pinene, *n*-decane, and *n*-dodecane) and various OS-related precursor mixtures (their yields will be discussed in the following section) is shown in Figs. 4c and d. The F_{aerosol} are very similar to each other in the presence of AS seed particles regardless of the precursor, accounting for ~95% of the LVOC fate at less than 1 photochemical day and ~70% at ~16 photochemical days. Conversely, the range of F_{aerosol} is much wider for non-seeded experiments (Figs. 4c and d), from ~40% to 80%. The results suggest that the OFR experiments under the seeded conditions here are the most relevant to the ambient atmosphere, particularly at less than 4 photochemical days, with yields potentially requiring a relatively small upwards adjustment (~30%) even at >14 photochemical days. The model also suggests that the impact of fragmentation reactions on SOA yields (derived from this OFR), when translated to the atmosphere, is likely to be very small, as the OH reactions of LVOC never dominate the overall fate (Fig. 4b).

Given the results of Fig. 4, future OFR studies investigating SOA yields should be conducted in the presence of pre-existing seed particles to reduce uncertainties, as theoretically suggested previously (Palm et al., 2016). The estimated fate of

LVOCs for seeded experiments here is used to apply an upwards correction to α -pinene (Fig. S8) and OS derived SOA yields (discussed in Sect. 3.2) assuming an LVOCs fraction of 80% in SOA (see Sect. S6 of the Supplement for details). As OH concentrations in smog chambers are generally much lower than studies with the OFRs, the LVOCs in smog chamber will mostly condense on aerosols, which is similar to the real atmosphere. Hence, when comparing the OFR yields to smog chambers, an LVOC fate correction should be applied. As shown in Fig. S8, the SOA yields from α -pinene in the current OFR after correction are in good agreement with previous smog chamber results despite the lower SOA mass concentration and precursor concentration.

3.2 SOA yields of OS-related precursors

The ECCC-OFR was used to investigate the SOA yields of complex precursor mixtures, specifically those derived from OS sources (see Methods). The SOA yields of these OS-related precursor mixtures are shown in Fig. 5a for unseeded experiments performed in an atmospherically relevant SOA mass concentration range ($< 50 \mu\text{g m}^{-3}$; Table 1). The SOA yield in this case is defined similarly to that in Sect. 3.1.2, but accounting for the calculated H/C ratio (Table S1) and measured carbon number distribution of emissions (Fig. 1a), as described in detail in Sect. S5 of the Supplement. Briefly, the H/C ratios of precursors were used to calculate the initial precursor mass concentrations from the measured total carbon concentration. The reacted mass concentrations were calculated using the rate constant with OH of corresponding *n*-alkanes that have the same carbon number as the average value of carbon number distributions. As demonstrated in Fig. 5a, the freshly mined OS ore results in the highest yields among the five precursor mixtures, with a maximum of 0.44 ± 0.05 at approximately 11 atmospheric equivalent photochemical days ($1.4 \times 10^{12} \text{ molecules cm}^{-3} \text{ s OH exposure}$, corresponding to approximately 1.6 days in OS plumes (Liggio et al., 2016)), followed by processed bitumen, with slightly lower yields over the entire range of photochemical age (with a maximum of 0.35 ± 0.03). The SOA yields of naphtha, dilbit and tailings pond emissions are significantly lower, with maximum SOA yields of approximately 0.1 ± 0.01 to 0.13 ± 0.01 . The difference in yields between source mixtures (Fig. 5a) can be qualitatively explained by the volatility distributions (VD) of these precursors (Fig. 1), with precursors of lower volatility (higher carbon number) having higher SOA yields (Lim and Ziemann, 2005; Lim and Ziemann, 2009). In this case, naphtha solvent and OS ore emissions represent volatility endpoints (high and low respectively) with other precursor mixtures being derived from a combination of these (see Sect. S4 of the Supplement for details). Although these precursors have very different SOA yields, their AMS mass spectra (Fig. S9) are similar, indicating a similar main precursor composition (alkanes).

SOA yields from several straight chain pure compounds (C_7 , C_{10} , and C_{12}) were also investigated in the ECCC-OFR to provide additional information on the nature of the OS related precursor mixtures, and are depicted in Fig. 5a. These single compounds were selected for comparison based upon the VD of the OS precursors (Fig. 1a), where heptane (C_7) represents the maximum of the VD of naphtha and dilbit, decane (C_{10}) the approximate average volatility of OS ore (see Sect. S4 of the Supplement) and dodecane (C_{12}) a compound representative of the lower end of the VD of OS ore and processed bitumen. As shown in Fig. 5a, despite naphtha and dilbit vapors being dominated by compounds with an equivalent volatility to heptane (Fig. 1a), their SOA yields (0.11 ± 0.01) are significantly higher than that of heptane (0.044 ± 0.006). Similarly, OS ore

emissions result in higher yields than decane, despite a comparable volatility, but lower yields than C₁₂. This suggests that alkanes with higher carbon number (and hence lower volatility and higher yield) contribute disproportionately to the overall SOA yields, relative to their proportions in the precursor emissions (Fig. 1a). Alternatively, cyclic hydrocarbons in the OS-related precursors could also contribute significantly to the overall yields, as experiments for cyclodecane and decalin (a bicyclic C₁₀ alkane) (Fig. 5a) result in much higher yields than decane. This is consistent with previous studies that demonstrated that cyclic alkanes have much higher yields than *n*-alkanes in general (Lim and Ziemann, 2009; Tkacik et al., 2012; Hunter et al., 2014). While the yields for single species alone cannot be used to distinguish between the contributions of cyclic and acyclic compounds to the observed OS derived SOA, elemental ratios of the SOA suggest that cyclic species may be an important contributor (see Sect. 3.3).

10 The SOA carbon and oxygen yields (Y_C and Y_O) for the least and most volatile precursor mixtures (OS ore and naphtha solvent respectively) are shown in Fig. 5b, as an indicator of the impact of fragmentation on the derived SOA yields. Both Y_C and Y_O for OS ore and naphtha reach a maximum at approximately 11 equivalent photochemical days, and then decrease with increasing photochemical age. The decrease in Y_O for OS ore and naphtha is ~1% per equivalent day from 11 to ~15-17 days. However, the Y_C for OS ore and naphtha decrease ~2%-4% per day, which is higher than the decrease in Y_O . This suggests
15 that fragmentation reactions increasingly influence SOA yields at higher photochemical ages for OS-related precursors, although a significant relationship between the degree of fragmentation and carbon number cannot be determined. Regardless, the overall impact of the competition between functionalization and fragmentation on the SOA yields here is small across all OS derived precursors. This is in contrast to other types of fuel products, specifically diesel and Southern Louisiana crude oil (Fig. 5b), which were shown to have SOA yields that are highly affected by fragmentation reactions (Lambe et al., 2012),
20 although those studies were likely impacted by wall losses.

The results of experiments conducted using 20 $\mu\text{g m}^{-3}$ solid ammonium sulfate (AS) seed particles are shown in Fig. 5c. Experiments with 10 and 40 $\mu\text{g m}^{-3}$ AS seed particles were also performed for OS ore and naphtha, but exhibited no SOA yield dependence on seed concentration (not shown), with the same SOA yields derived in all cases. Generally, the SOA yields for all precursors are enhanced significantly in the presence of AS seed particles, with maximum yields of 0.58 ± 0.03 and
25 0.18 ± 0.02 for the least and most volatile OS precursors. This effect is more clearly depicted as a yield enhancement ratio ($Y_{\text{seeded}}/Y_{\text{unseeded}}$) in Fig. 6. Based upon Fig. 6, it is evident that SOA from precursors with higher volatilities are more impacted by the presence of AS seed particles; SOA yield enhancement ratios for naphtha and dilbit (~60%) are higher than OS ore and bitumen (~30%) after approximately 2 equivalent photochemical days, with that of tailings pond SOA between them. It is also evident that the enhancement factor is somewhat larger during the initial stages of oxidation (up to >100% at <2 equivalent
30 photochemical days). This is likely a result of the different LVOCs fate for seeded and unseeded experiments. As shown in Sect. 3.1.3 and Fig. 4d, the fraction of LVOCs that condense on aerosol (F_{aerosol}) at <2 equivalent photochemical days for unseeded experiments is much lower than that for seeded experiments, which will lead to a larger yield enhancement ratio in the presence of seed particles. The finding that the presence of seeds can enhance the SOA yields is in agreement with various previous work (Kroll et al., 2007; Hildebrandt et al., 2009; Zhang et al., 2014; Lambe et al., 2015; Li et al., 2018). In addition to

the difference in LVOCs fate discussed above, the enhanced SOA yield in the presence of seed particles can also be due to increased aerosol surface area that competes with other sinks (e.g., vapor wall losses for smog chambers) and enhances the gas-particle partitioning of S/IVOCs, as suggested previously (Hildebrandt et al., 2009; Zhang et al., 2014; Li et al., 2018).

The OS precursor SOA yields for seeded experiments are adjusted upwards to account for the fate of formed LVOCs through normalization by the F_{aerosol} above (Sect. 3.1.3), with the results of this correction shown in Fig. 5d. Here, we assume 80% of the SOA is LVOCs, while the other 20% is S/IVOCs (see Sect. S6 of the Supplement for details). Relative to the yields of Fig. 5c, the LVOCs fate adjusted SOA yields of Fig. 5d are ~4% to 37% larger for all precursors, depending upon the OH exposure. As noted above, the fate of LVOC in seeded experiments is primarily condensation to the aerosols, requiring a relatively small adjustment. As a result, the seeded experiment data in Fig. 5d represent our best estimate of the SOA yields for the precursors, applicable to the ambient atmosphere (under these conditions). In this case, the maximum SOA yield for the least and most volatile precursor mixtures (OS ore and naphtha) increased from 0.58 ± 0.03 to 0.71 ± 0.04 and 0.18 ± 0.02 to 0.23 ± 0.02 respectively after adjustment (Fig. 5d). In addition, applying an LVOC fate adjustment results in SOA yields for most OS precursors, α -pinene, and *n*-alkanes generally increasing with increasing OH exposure (Fig. S8 and Fig. 5d). This further suggests, as noted above, that the fragmentation reactions will not significantly decrease the SOA yields for these species in the ambient atmosphere, even after 16 equivalent photochemical days. However, uncertainties still remain when using OFRs to simulate the SOA formation processes in the real atmosphere, likely from differing fates of intermediate radicals (e.g., RO₂) especially at high OH exposure as suggested very recently (Peng et al., 2019).

3.3 Elemental ratios of OS-related SOA

The elemental H/C and O/C ratios of SOA particles are illustrated in a Van Krevelen diagram (Heald et al., 2010) in Fig. 7. Figure 7 indicates that the elemental ratios of SOA from OS ore and bitumen (and its photochemical evolution) are very similar (O/C: 0.45-0.8, H/C: 1.4-1.6), as are the elemental ratios of SOA formed from naphtha, dilbit and tailings pond water (O/C: 0.6-0.9, H/C: 1.5-1.7). This is analogous to the similarity in the yields between the same precursors as discussed above (Fig. 5) and consistent with the volatility of the precursors (Fig. 1). The lower O/C ratios of OS ore and bitumen SOA is probably due to their larger molecular size, with higher carbon number (i.e., lower volatility) precursors requiring less oxygen (hence fewer oxidation steps) to partition into the particle phase (Tkacik et al., 2012). The H/C ratios are also lower for SOA formed from lower volatility precursor mixtures, which is likely a result of different H/C of the precursors, with generally lower H/C for higher carbon number hydrocarbons. Assuming a linear relationship in Fig. 7, the y-intercept is indicative of the average H/C of the precursor mixture (Fig. S10). The intercept of naphtha and dilbit SOA (~2.1) is higher than OS ore and bitumen SOA (~1.8), indicating a higher H/C ratio for those precursors.

Similar inferences are made when comparing the evolution of the elemental ratios of SOA from various single alkane species in Van Krevelen space to that of OS precursors (Fig. 7). For example, SOA from parent *n*-alkanes with successively higher carbon number (and lower volatility) move towards the bottom-left of the Van Krevelen diagram. However, the position of OS-related SOA in Van Krevelen space is not consistent with the corresponding *n*-alkanes; naphtha, dilbit and tailings SOA

reside below *n*-heptane (C₇), despite having a very similar volatility (Fig. 1a). Similarly, OS ore and bitumen, reside below *n*-dodecane (C₁₂), despite C₁₂ volatility compounds contributing little to the overall volatility distribution of precursors (Fig. 1a). This discrepancy may be explained by the contribution of cyclic alkanes, since SOA formed from cyclic structures tend to reside below acyclic alkane SOA in Van Krevelen space, and near that of OS derived SOA (e.g., cyclodecane and decalin relative to decane SOA and OS ore SOA in Fig. 7). Recent aircraft measurement indicated that the cycloalkanes contribute 13%-27% of the total alkanes (Li et al., 2017) for Suncor and CNRL facilities (where the OS samples were collected), which will contribute a large proportion of SOA after considering their high SOA yields (Figs. 5a, c and d). A lower H/C ratio for SOA derived from cyclic alkanes is consistent with the parent hydrocarbon having lower H/C. The linear regression results of H/C vs O/C for alkane precursors are listed in Table S1, from which the relationship between precursor H/C and intercept is obtained (see Sect. S5 in the Supplement for details). A comparison between the H/C ratios of alkanes and OS precursors demonstrates that the H/C ratios of the OS precursors are generally lower than that of the corresponding *n*-alkane (e.g., ~2.2 for naphtha and dilbit, ~2.3 for C₇; ~2 for OS ore, ~2.2 for C₁₀), likely from the contribution of cyclic alkanes. Aromatics may also play a role in the decrease of H/C ratio of precursors; however, their contributions are likely small according to recent aircraft measurement by Li et al. (2017) (e.g., 3.7% aromatics compared to alkanes for CNRL). In addition, the presence of aromatics will not decrease the observed H/C and O/C of SOA, for example, the H/C and O/C of toluene SOA (1.67 and 0.85) (Canagaratna et al., 2015) is similar to that of heptane SOA observed here. While the current data cannot quantitatively apportion OS precursors to various structures (cyclic vs *n*-alkane/branched), the above Van Krevelen analysis suggests that cyclic compounds are an important contributor to the observed SOA.

The locations of two broad types of SOA, SV-OOA and LV-OOA (semi-volatile and low volatility oxidized organic aerosol) from various studies (Ng et al., 2011; Canagaratna et al., 2015), and that of the SOA downwind of the oil sands from previous aircraft measurements (Liggio et al., 2016) in Van Krevelen space are also shown in Fig. 7. The positions of SOA formed from OS-related precursors in the ECCC-OFR are generally in the range of previous ambient OOA. They are in good agreement with SV-OOA and LV-OOA for experiments simulating ~2 photochemical days (~2.6×10¹¹ molecules cm⁻³ s OH exposure) and ~2 weeks (~2 ×10¹² molecules cm⁻³ s OH exposure), respectively. Furthermore, OS ore and bitumen derived SOA are more similar to ambient SV-OOA and LV-OOA than naphtha, dilbit and tailings pond water derived SOA (Fig. 7). This highlights the contribution of intermediate-volatility alkanes to ambient SOA in the oil sands, particularly since the SOA formed from OS ore and bitumen are in good agreement with the aircraft data (Liggio et al., 2016) (Fig. 7). Hence, these results indicate that low-volatility precursors from open-pit mining sources (i.e., OS ore) are likely the largest contributors to the SOA formed downwind of the Alberta OS region, while precursors of high volatility play a minor role, likely due to their lower SOA yields.

4 Conclusions and implications

In this study, a newly designed oxidation flow reactor (ECCC-OFR) was applied to the investigation of SOA formation from single precursor compounds (α -pinene, *n*-alkanes, and cyclic alkanes) and complex mixtures (OS-related precursors). The SOA yields for α -pinene and alkanes obtained in the ECCC-OFR are similar to previous smog chamber studies but significantly higher than other OFRs. The current results provide SOA yield information for alkane precursors for which limited data are available especially at moderate to high photochemical ages (Tkacik et al., 2012; Lambe et al., 2012). In addition, the differences in yields between the current and other OFRs suggests that while OFRs can provide insight into SOA mechanisms, care must be taken in deriving quantitative results from OFRs, which are often designed with slightly different geometries and operated under a variety of conditions. For example, recent OFR modeling results (Peng et al., 2019) demonstrated that the working conditions (e.g., light intensity and wavelength, humidity and external OH reactivity) could influence the RO₂ fate and result in less atmospherically relevant chemical mechanisms for SOA formation in the OFR.

Variability in the qualitative/mechanistic SOA information derived from OFRs is also possible. In particular, previous OFR studies (Lambe et al., 2012; Chen et al., 2013; Tkacik et al., 2014; Lambe et al., 2015; Ortega et al., 2016; Palm et al., 2016) have attributed large decreases in SOA yields at moderate to high photochemical age (typically after 4-5 equivalent days) to the dominant role of gas-phase fragmentation reactions. However, the current study indicates that the impact of fragmentation on SOA yields from various sources is minimal in the ECCC-OFR, likely due to reduced wall losses relative to other OFRs, whose fluid dynamics are not entirely laminar as suggested previously (Huang et al., 2017; Mitroo et al., 2018). Accounting for the fate of LVOCs (Palm et al., 2016) in the ECCC-OFR further indicates that the impact of fragmentation on SOA yields in the ambient atmosphere will be even smaller than that within the OFR. This implies that modeling SOA formation to include the impacts of fragmentation should be carefully evaluated, especially if using OFR data to provide empirical factors for fragmentation (Chen et al., 2013). However, the current data also indicate that the impact of fragmentation on SOA yields in OFRs can be significantly reduced through the use of seed particles, which increase the fraction of LVOCs which condense on aerosols (F_{aerosol}). This suggests that future laboratory OFR experiments studying SOA yields should be conducted with seed particles to obtain more relevant qualitative and quantitative data.

Application of the ECCC-OFR to OS-related precursor mixtures indicates that lower volatility OS ore and bitumen vapors have significantly higher yields (maximum of ~0.6-0.7 for seeded experiments after LVOCs fate correction) than those from higher volatility naphtha, dilbit and tailings pond vapors (maximum of ~0.2-0.3 under the same conditions). The relatively high SOA yields from OS ore, together with the similar elemental ratios between ambient measurements and OFR experiments, is consistent with open-pit mining activities being the largest contributor to the observed SOA downwind of the oil sands operations (Liggio et al., 2016). The SOA yields and elemental ratio analysis also suggest that cyclic alkanes are important contributors to OS-related SOA. The OS SOA information derived here, for the range of precursor mixtures encountered in the oil sands, can be used to improve parameterizations of SOA for the OS region through source specific inputs of SOA precursor properties and SOA yields, and to evaluate the subsequent regional modeling of SOA (Stroud et al., 2018). The

attribution of observed industrial SOA in the oil sands to specific sources (i.e., OS ore emissions from open-pit mining) supports the potential for future mitigation strategies for reducing SOA from this sector.

Author contribution

KL and JL designed the OFR and the experiments; KL conducted the experiments; PL and KL measured the volatility
5 distributions; KL analyzed the data and wrote the paper with contributions from JL; PL, CH, QL, and SML commented on the manuscript.

Acknowledgements

The authors acknowledge funding support from the Air Pollution program of Environment and Climate Change Canada (ECCC), and the Oil Sands Monitoring program (OSM). We further thank the Canada's Oil Sands Innovation Alliance
10 (COSIA) for the organization and provision of oil sands related samples used in this paper.

References

- Alboudwarej, H., Felix, J., Taylor, S., Badry, R., Bremner, C., Brough, B., Skeates, C., Baker, A., Palmer, D., Pattison, K., Beshry, M., Krawchuk, P., Brown, G., Calvo, R., Canas Triana, J. A., Hathcock, R., Koerner, K., Hughes, T., Kundu, D., de C'ardenas, J. L., and West, C.: Highlighting heavy oil, *Oilfield Rev.*, 18, 34-53, 2006.
- 15 Atkinson, R., and Arey, J.: Atmospheric Degradation of Volatile Organic Compounds, *Chemical Reviews*, 103, 4605-4638, 10.1021/cr0206420, 2003.
- Bruns, E. A., El Haddad, I., Keller, A., Klein, F., Kumar, N. K., Pieber, S. M., Corbin, J. C., Slowik, J. G., Brune, W. H., Baltensperger, U., and Prévôt, A. S. H.: Inter-comparison of laboratory smog chamber and flow reactor systems on organic aerosol yield and composition, *Atmospheric Measurement Techniques*, 8, 2315-2332, 10.5194/amt-8-2315-2015, 2015.
- 20 Canagaratna, M. R., Jimenez, J. L., Kroll, J. H., Chen, Q., Kessler, S. H., Massoli, P., Hildebrandt Ruiz, L., Fortner, E., Williams, L. R., Wilson, K. R., Surratt, J. D., Donahue, N. M., Jayne, J. T., and Worsnop, D. R.: Elemental ratio measurements of organic compounds using aerosol mass spectrometry: characterization, improved calibration, and implications, *Atmospheric Chemistry and Physics*, 15, 253-272, 10.5194/acp-15-253-2015, 2015.
- 25 Chen, S., Brune, W. H., Lambe, A. T., Davidovits, P., and Onasch, T. B.: Modeling organic aerosol from the oxidation of α -pinene in a Potential Aerosol Mass (PAM) chamber, *Atmospheric Chemistry and Physics*, 13, 5017-5031, 10.5194/acp-13-5017-2013, 2013.
- Donahue, N. M., Robinson, A. L., Stanier, C. O., and Pandis, S. N.: Coupled partitioning, dilution, and chemical aging of semivolatile organics, *Environmental science & technology*, 40, 2635-2643, 10.1021/es052297c, 2006.
- 30 Donahue, N. M., Kroll, J. H., Pandis, S. N., and Robinson, A. L.: A two-dimensional volatility basis set – Part 2: Diagnostics of organic-aerosol evolution, *Atmospheric Chemistry and Physics*, 12, 615-634, 10.5194/acp-12-615-2012, 2012.
- Eddingsaas, N. C., Loza, C. L., Yee, L. D., Chan, M., Schilling, K. A., Chhabra, P. S., Seinfeld, J. H., and Wennberg, P. O.: α -pinene photooxidation under controlled chemical conditions – Part 2: SOA yield and composition in low- and high-NO_x environments, *Atmospheric Chemistry and Physics*, 12, 7413-7427, 10.5194/acp-12-7413-2012, 2012.
- 35 Hallquist, M., Wenger, J. C., Baltensperger, U., Rudich, Y., Simpson, D., Claeys, M., Dommen, J., Donahue, N. M., George, C., Goldstein, A. H., Hamilton, J. F., Herrmann, H., Hoffmann, T., Iinuma, Y., Jang, M., Jenkin, M. E., Jimenez, J. L.,

- Kiendler-Scharr, A., Maenhaut, W., McFiggans, G., Mentel, T. F., Monod, A., Prevot, A. S. H., Seinfeld, J. H., Surratt, J. D., Szmigielski, R., and Wildt, J.: The formation, properties and impact of secondary organic aerosol: current and emerging issues, *Atmospheric Chemistry and Physics*, 9, 5155-5236, 2009.
- 5 Han, Y., Stroud, C. A., Liggio, J., and Li, S.-M.: The effect of particle acidity on secondary organic aerosol formation from α -pinene photooxidation under atmospherically relevant conditions, *Atmospheric Chemistry and Physics*, 16, 13929-13944, 10.5194/acp-16-13929-2016, 2016.
- 10 Harner, T., Rauert, C., Muir, D., Schuster, J. K., Hsu, Y.-M., Zhang, L., Marson, G., Watson, J. G., Ahad, J., Cho, S., Jariyasopit, N., Kirk, J., Korosi, J., Landis, M. S., Martin, J. W., Zhang, Y., Fernie, K., Wentworth, G. R., Wnorowski, A., Dabek, E., Charland, J.-P., Pauli, B., Wania, F., Galarneau, E., Cheng, I., Makar, P., Whaley, C., Chow, J. C., and Wang, X.: Air synthesis review: polycyclic aromatic compounds in the oil sands region, *Environmental Reviews*, 26, 430-468, 10.1139/er-2018-0039, 2018.
- 15 Heald, C. L., Kroll, J. H., Jimenez, J. L., Docherty, K. S., DeCarlo, P. F., Aiken, A. C., Chen, Q., Martin, S. T., Farmer, D. K., and Artaxo, P.: A simplified description of the evolution of organic aerosol composition in the atmosphere, *Geophysical Research Letters*, 37, 10.1029/2010gl042737, 2010.
- Hildebrandt, L., Donahue, N. M., and Pandis, S. N.: High formation of secondary organic aerosol from the photo-oxidation of toluene, *Atmospheric Chemistry and Physics*, 9, 2973-2986, 2009.
- Hofzumahaus, A., Rohrer, F., Lu, K., Bohn, B., Brauers, T., Chang, C.-C., Fuchs, H., Holland, F., Kita, K., Kondo, Y., Li, X., Lou, S., Shao, M., Zeng, L., Wahner, A., and Zhang, Y.: Amplified Trace Gas Removal in the Troposphere, *Science*, 324, 1702-1704, 10.1126/science.1164566, 2009.
- 20 Huang, Y., Coggon, M. M., Zhao, R., Lignell, H., Bauer, M. U., Flagan, R. C., and Seinfeld, J. H.: The Caltech Photooxidation Flow Tube reactor: design, fluid dynamics and characterization, *Atmospheric Measurement Techniques*, 10, 839-867, 10.5194/amt-10-839-2017, 2017.
- Hunter, J. F., Carrasquillo, A. J., Daumit, K. E., and Kroll, J. H.: Secondary organic aerosol formation from acyclic, monocyclic, and polycyclic alkanes, *Environmental science & technology*, 48, 10227-10234, 10.1021/es502674s, 2014.
- 25 Ihalainen, M., Tiitta, P., Czech, H., Yli-Pirilä, P., Hartikainen, A., Kortelainen, M., Tissari, J., Stengel, B., Sklorz, M., Suhonen, H., Lamberg, H., Leskinen, A., Kiendler-Scharr, A., Harndorf, H., Zimmermann, R., Jokiniemi, J., and Sippula, O.: A novel high-volume Photochemical Emission Aging flow tube Reactor (PEAR), *Aerosol Science and Technology*, 53, 276-294, 10.1080/02786826.2018.1559918, 2019.
- Jathar, S. H., Friedman, B., Galang, A. A., Link, M. F., Brophy, P., Volckens, J., Eluri, S., and Farmer, D. K.: Linking Load, Fuel, and Emission Controls to Photochemical Production of Secondary Organic Aerosol from a Diesel Engine, *Environmental science & technology*, 51, 1377-1386, 10.1021/acs.est.6b04602, 2017.
- 30 Jimenez, J. L., Canagaratna, M. R., Donahue, N. M., Prevot, A. S., Zhang, Q., Kroll, J. H., DeCarlo, P. F., Allan, J. D., Coe, H., Ng, N. L., Aiken, A. C., Docherty, K. S., Ulbrich, I. M., Grieshop, A. P., Robinson, A. L., Duplissy, J., Smith, J. D., Wilson, K. R., Lanz, V. A., Hueglin, C., Sun, Y. L., Tian, J., Laaksonen, A., Raatikainen, T., Rautiainen, J., Vaattovaara, P., Ehn, M., Kulmala, M., Tomlinson, J. M., Collins, D. R., Cubison, M. J., Dunlea, E. J., Huffman, J. A., Onasch, T. B., Alfarra, M. R., Williams, P. I., Bower, K., Kondo, Y., Schneider, J., Drewnick, F., Borrmann, S., Weimer, S., Demerjian, K., Salcedo, D., Cottrell, L., Griffin, R., Takami, A., Miyoshi, T., Hatakeyama, S., Shimono, A., Sun, J. Y., Zhang, Y. M., Dzepina, K., Kimmel, J. R., Sueper, D., Jayne, J. T., Herndon, S. C., Trimborn, A. M., Williams, L. R., Wood, E. C., Middlebrook, A. M., Kolb, C. E., Baltensperger, U., and Worsnop, D. R.: Evolution of organic aerosols in the atmosphere, *Science*, 326, 1525-1529, 10.1126/science.1180353, 2009.
- 40 Jung, K., Ok, Y. S., and Chang, S. X.: Sulfate adsorption properties of acid-sensitive soils in the Athabasca oil sands region in Alberta, Canada, *Chemosphere*, 84, 457-463, 10.1016/j.chemosphere.2011.03.034, 2011.
- Kang, E., Root, M. J., Toohey, D. W., and Brune, W. H.: Introducing the concept of Potential Aerosol Mass (PAM), *Atmospheric Chemistry and Physics*, 7, 5727-5744, 2007.
- 45 Kang, E., Toohey, D. W., and Brune, W. H.: Dependence of SOA oxidation on organic aerosol mass concentration and OH exposure: experimental PAM chamber studies, *Atmospheric Chemistry and Physics*, 11, 1837-1852, 10.5194/acp-11-1837-2011, 2011.
- Karjalainen, P., Timonen, H., Saukko, E., Kuuluvainen, H., Saarikoski, S., Aakko-Saksa, P., Murtonen, T., Bloss, M., Dal Maso, M., Simonen, P., Ahlberg, E., Svenningsson, B., Brune, W. H., Hillamo, R., Keskinen, J., and Rönkkö, T.: Time-

- resolved characterization of primary particle emissions and secondary particle formation from a modern gasoline passenger car, *Atmospheric Chemistry and Physics*, 16, 8559-8570, 10.5194/acp-16-8559-2016, 2016.
- 5 Kirk, J. L., Muir, D. C., Gleason, A., Wang, X., Lawson, G., Frank, R. A., Lehnherr, I., and Wrona, F.: Atmospheric deposition of mercury and methylmercury to landscapes and waterbodies of the Athabasca oil sands region, *Environmental science & technology*, 48, 7374-7383, 10.1021/es500986r, 2014.
- Kroll, J. H., Chan, A. W. H., Ng, N. L., Flagan, R. C., and Seinfeld, J. H.: Reactions of semivolatile organics and their effects on secondary organic aerosol formation, *Environmental science & technology*, 41, 3545-3550, 10.1021/es062059x, 2007.
- 10 Kroll, J. H., and Seinfeld, J. H.: Chemistry of secondary organic aerosol: Formation and evolution of low-volatility organics in the atmosphere, *Atmospheric Environment*, 42, 3593-3624, 10.1016/j.atmosenv.2008.01.003, 2008.
- Kroll, J. H., Smith, J. D., Che, D. L., Kessler, S. H., Worsnop, D. R., and Wilson, K. R.: Measurement of fragmentation and functionalization pathways in the heterogeneous oxidation of oxidized organic aerosol, *Physical Chemistry Chemical Physics*, 11, 8005-8014, 10.1039/b905289e, 2009.
- 15 Lambe, A., Massoli, P., Zhang, X., Canagaratna, M., Nowak, J., Daube, C., Yan, C., Nie, W., Onasch, T., Jayne, J., Kolb, C., Davidovits, P., Worsnop, D., and Brune, W.: Controlled nitric oxide production via $O(^1D) + N_2O$ reactions for use in oxidation flow reactor studies, *Atmospheric Measurement Techniques*, 10, 2283-2298, 10.5194/amt-10-2283-2017, 2017.
- Lambe, A. T., Ahern, A. T., Williams, L. R., Slowik, J. G., Wong, J. P. S., Abbatt, J. P. D., Brune, W. H., Ng, N. L., Wright, J. P., Croasdale, D. R., Worsnop, D. R., Davidovits, P., and Onasch, T. B.: Characterization of aerosol photooxidation flow reactors: heterogeneous oxidation, secondary organic aerosol formation and cloud condensation nuclei activity measurements, *Atmospheric Measurement Techniques*, 4, 445-461, 10.5194/amt-4-445-2011, 2011.
- 20 Lambe, A. T., Onasch, T. B., Croasdale, D. R., Wright, J. P., Martin, A. T., Franklin, J. P., Massoli, P., Kroll, J. H., Canagaratna, M. R., Brune, W. H., Worsnop, D. R., and Davidovits, P.: Transitions from functionalization to fragmentation reactions of laboratory secondary organic aerosol (SOA) generated from the OH oxidation of alkane precursors, *Environmental science & technology*, 46, 5430-5437, 10.1021/es300274t, 2012.
- 25 Lambe, A. T., Chhabra, P. S., Onasch, T. B., Brune, W. H., Hunter, J. F., Kroll, J. H., Cummings, M. J., Brogan, J. F., Parmar, Y., Worsnop, D. R., Kolb, C. E., and Davidovits, P.: Effect of oxidant concentration, exposure time, and seed particles on secondary organic aerosol chemical composition and yield, *Atmospheric Chemistry and Physics*, 15, 3063-3075, 10.5194/acp-15-3063-2015, 2015.
- 30 Li, K., Li, J., Wang, W., Li, J., Peng, C., Wang, D., and Ge, M.: Effects of Gas-Particle Partitioning on Refractive Index and Chemical Composition of m-Xylene Secondary Organic Aerosol, *The Journal of Physical Chemistry A*, 122, 3250-3260, 10.1021/acs.jpca.7b12792, 2018.
- Li, R., Palm, B. B., Ortega, A. M., Hlywiak, J., Hu, W., Peng, Z., Day, D. A., Knote, C., Brune, W. H., de Gouw, J. A., and Jimenez, J. L.: Modeling the radical chemistry in an oxidation flow reactor: radical formation and recycling, sensitivities, and the OH exposure estimation equation, *The journal of physical chemistry. A*, 119, 4418-4432, 10.1021/jp509534k, 2015.
- 35 Li, S.-M., Leithead, A., Moussa, S. G., Liggio, J., Moran, M. D., Wang, D., Hayden, K., Darlington, A., Gordon, M., Staebler, R., Makar, P. A., Stroud, C. A., McLaren, R., Liu, P. S. K., O'Brien, J., Mittermeier, R. L., Zhang, J., Marson, G., Cober, S. G., Wolde, M., and Wentzell, J. J. B.: Differences between measured and reported volatile organic compound emissions from oil sands facilities in Alberta, Canada, *Proceedings of the National Academy of Sciences*, 114, E3756-E3765, 10.1073/pnas.1617862114, 2017.
- 40 Liggio, J., Li, S. M., Hayden, K., Taha, Y. M., Stroud, C., Darlington, A., Drollette, B. D., Gordon, M., Lee, P., Liu, P., Leithead, A., Moussa, S. G., Wang, D., O'Brien, J., Mittermeier, R. L., Brook, J. R., Lu, G., Staebler, R. M., Han, Y., Tokarek, T. W., Osthoff, H. D., Makar, P. A., Zhang, J., Plata, D. L., and Gentner, D. R.: Oil sands operations as a large source of secondary organic aerosols, *Nature*, 534, 91-94, 10.1038/nature17646, 2016.
- 45 Lim, Y. B., and Ziemann, P. J.: Products and mechanism of secondary organic aerosol formation from reactions of n-alkanes with OH radicals in the presence of NO_x, *Environmental science & technology*, 39, 9229-9236, 10.1021/es051447g, 2005.

- Lim, Y. B., and Ziemann, P. J.: Effects of Molecular Structure on Aerosol Yields from OH Radical-Initiated Reactions of Linear, Branched, and Cyclic Alkanes in the Presence of NO_x, *Environmental science & technology*, 43, 2328-2334, 10.1021/es803389s, 2009.
- 5 Liu, Y., Liggió, J., Harner, T., Jantunen, L., Shoeib, M., and Li, S. M.: Heterogeneous OH initiated oxidation: a possible explanation for the persistence of organophosphate flame retardants in air, *Environmental science & technology*, 48, 1041-1048, 10.1021/es404515k, 2014.
- Loza, C. L., Craven, J. S., Yee, L. D., Coggon, M. M., Schwantes, R. H., Shiraiwa, M., Zhang, X., Schilling, K. A., Ng, N. L., Canagaratna, M. R., Ziemann, P. J., Flagan, R. C., and Seinfeld, J. H.: Secondary organic aerosol yields of 12-carbon alkanes, *Atmospheric Chemistry and Physics*, 14, 1423-1439, 10.5194/acp-14-1423-2014, 2014.
- 10 Makar, P. A., Akingunola, A., Aherne, J., Cole, A. S., Aklilu, Y.-a., Zhang, J., Wong, I., Hayden, K., Li, S.-M., Kirk, J., Scott, K., Moran, M. D., Robichaud, A., Cathcart, H., Baratzedah, P., Pabla, B., Cheung, P., Zheng, Q., and Jeffries, D. S.: Estimates of exceedances of critical loads for acidifying deposition in Alberta and Saskatchewan, *Atmospheric Chemistry and Physics*, 18, 9897-9927, 10.5194/acp-18-9897-2018, 2018.
- 15 Mao, J., Ren, X., Brune, W. H., Olson, J. R., Crawford, J. H., Fried, A., Huey, L. G., Cohen, R. C., Heikes, B., Singh, H. B., Blake, D. R., Sachse, G. W., Diskin, G. S., Hall, S. R., and Shetter, R. E.: Airborne measurement of OH reactivity during INTEX-B, *Atmospheric Chemistry and Physics*, 9, 163-173, 2009.
- Mitroo, D., Sun, Y., Combet, D. P., Kumar, P., and Williams, B. J.: Assessing the degree of plug flow in oxidation flow reactors (OFRs): a study on a potential aerosol mass (PAM) reactor, *Atmospheric Measurement Techniques*, 11, 1741-1756, 10.5194/amt-11-1741-2018, 2018.
- 20 Mohr, S. H., and Evans, G. M.: Long term prediction of unconventional oil production, *Energy Policy*, 38, 265-276, 10.1016/j.enpol.2009.09.015, 2010.
- Ng, N. L., Chhabra, P. S., Chan, A. W. H., Surratt, J. D., Kroll, J. H., Kwan, A. J., McCabe, D. C., Wennberg, P. O., Sorooshian, A., Murphy, S. M., Dalleska, N. F., Flagan, R. C., and Seinfeld, J. H.: Effect of NO(x) level on secondary organic aerosol (SOA) formation from the photooxidation of terpenes, *Atmospheric Chemistry and Physics*, 7, 5159-5174, 25 2007.
- Ng, N. L., Canagaratna, M. R., Jimenez, J. L., Chhabra, P. S., Seinfeld, J. H., and Worsnop, D. R.: Changes in organic aerosol composition with aging inferred from aerosol mass spectra, *Atmospheric Chemistry and Physics*, 11, 6465-6474, 10.5194/acp-11-6465-2011, 2011.
- Odum, J. R., Hoffmann, T., Bowman, F., Collins, D., Flagan, R. C., and Seinfeld, J. H.: Gas/particle partitioning and secondary organic aerosol yields, *Environmental science & technology*, 30, 2580-2585, 10.1021/es950943+, 1996.
- 30 Ortega, A. M., Day, D. A., Cubison, M. J., Brune, W. H., Bon, D., de Gouw, J. A., and Jimenez, J. L.: Secondary organic aerosol formation and primary organic aerosol oxidation from biomass-burning smoke in a flow reactor during FLAME-3, *Atmospheric Chemistry and Physics*, 13, 11551-11571, 10.5194/acp-13-11551-2013, 2013.
- Ortega, A. M., Hayes, P. L., Peng, Z., Palm, B. B., Hu, W., Day, D. A., Li, R., Cubison, M. J., Brune, W. H., Graus, M., 35 Warneke, C., Gilman, J. B., Kuster, W. C., de Gouw, J., Gutiérrez-Montes, C., and Jimenez, J. L.: Real-time measurements of secondary organic aerosol formation and aging from ambient air in an oxidation flow reactor in the Los Angeles area, *Atmospheric Chemistry and Physics*, 16, 7411-7433, 10.5194/acp-16-7411-2016, 2016.
- Owen, N. A., Inderwildi, O. R., and King, D. A.: The status of conventional world oil reserves—Hype or cause for concern?, *Energy Policy*, 38, 4743-4749, 10.1016/j.enpol.2010.02.026, 2010.
- 40 Palm, B. B., Campuzano-Jost, P., Ortega, A. M., Day, D. A., Kaser, L., Jud, W., Karl, T., Hansel, A., Hunter, J. F., Cross, E. S., Kroll, J. H., Peng, Z., Brune, W. H., and Jimenez, J. L.: In situ secondary organic aerosol formation from ambient pine forest air using an oxidation flow reactor, *Atmospheric Chemistry and Physics*, 16, 2943-2970, 10.5194/acp-16-2943-2016, 2016.
- Peng, Z., Palm, B. B., Day, D. A., Talukdar, R. K., Hu, W., Lambe, A. T., Brune, W. H., and Jimenez, J. L.: Model Evaluation of New Techniques for Maintaining High-NO Conditions in Oxidation Flow Reactors for the Study of OH-Initiated Atmospheric Chemistry, *ACS Earth and Space Chemistry*, 2, 72-86, 10.1021/acsearthspacechem.7b00070, 2018.
- 45 Peng, Z., Lee-Taylor, J., Orlando, J. J., Tyndall, G. S., and Jimenez, J. L.: Organic peroxy radical chemistry in oxidation flow reactors and environmental chambers and their atmospheric relevance, *Atmospheric Chemistry and Physics*, 19, 813-834, 10.5194/acp-19-813-2019, 2019.

- Simonen, P., Saukko, E., Karjalainen, P., Timonen, H., Bloss, M., Aakko-Saksa, P., Rönkkö, T., Keskinen, J., and Dal Maso, M.: A new oxidation flow reactor for measuring secondary aerosol formation of rapidly changing emission sources, *Atmospheric Measurement Techniques*, 10, 1519-1537, 10.5194/amt-10-1519-2017, 2017.
- 5 Simpson, I. J., Blake, N. J., Barletta, B., Diskin, G. S., Fuelberg, H. E., Gorham, K., Huey, L. G., Meinardi, S., Rowland, F. S., Vay, S. A., Weinheimer, A. J., Yang, M., and Blake, D. R.: Characterization of trace gases measured over Alberta oil sands mining operations: 76 speciated C₂–C₁₀ volatile organic compounds (VOCs), CO₂, CH₄, CO, NO, NO₂, NO_y, O₃ and SO₂, *Atmos. Chem. Phys.*, 10, 11931-11954, 10.5194/acp-10-11931-2010, 2010.
- 10 Stone, D., Whalley, L. K., and Heard, D. E.: Tropospheric OH and HO₂ radicals: field measurements and model comparisons, *Chemical Society reviews*, 41, 6348-6404, 10.1039/C2CS35140D, 2012.
- Stroud, C. A., Makar, P. A., Zhang, J., Moran, M. D., Akingunola, A., Li, S.-M., Leithead, A., Hayden, K., and Siu, M.: Improving air quality model predictions of organic species using measurement-derived organic gaseous and particle emissions in a petrochemical-dominated region, *Atmospheric Chemistry and Physics*, 18, 13531-13545, 10.5194/acp-18-13531-2018, 2018.
- 15 Tang, M. J., Shiraiwa, M., Pöschl, U., Cox, R. A., and Kalberer, M.: Compilation and evaluation of gas phase diffusion coefficients of reactive trace gases in the atmosphere: Volume 2. Diffusivities of organic compounds, pressure-normalised mean free paths, and average Knudsen numbers for gas uptake calculations, *Atmospheric Chemistry and Physics*, 15, 5585-5598, 10.5194/acp-15-5585-2015, 2015.
- Tkacik, D. S., Presto, A. A., Donahue, N. M., and Robinson, A. L.: Secondary organic aerosol formation from intermediate-volatility organic compounds: cyclic, linear, and branched alkanes, *Environmental science & technology*, 46, 8773-8781, 10.1021/es301112c, 2012.
- Tkacik, D. S., Lambe, A. T., Jathar, S., Li, X., Presto, A. A., Zhao, Y., Blake, D., Meinardi, S., Jayne, J. T., Croteau, P. L., and Robinson, A. L.: Secondary organic aerosol formation from in-use motor vehicle emissions using a potential aerosol mass reactor, *Environmental science & technology*, 48, 11235-11242, 10.1021/es502239v, 2014.
- 25 Tokarek, T. W., Odame-Ankrah, C. A., Huo, J. A., McLaren, R., Lee, A. K. Y., Adam, M. G., Willis, M. D., Abbatt, J. P. D., Mihele, C., Darlington, A., Mittermeier, R. L., Strawbridge, K., Hayden, K. L., Olfert, J. S., Schnitzler, E. G., Brownsey, D. K., Assad, F. V., Wentworth, G. R., Tevlin, A. G., Worthy, D. E. J., Li, S.-M., Liggio, J., Brook, J. R., and Osthoff, H. D.: Principal component analysis of summertime ground site measurements in the Athabasca oil sands with a focus on analytically unresolved intermediate-volatility organic compounds, *Atmospheric Chemistry and Physics*, 18, 17819-17841, 10.5194/acp-18-17819-2018, 2018.
- 30 Veres, P., Gilman, J. B., Roberts, J. M., Kuster, W. C., Warneke, C., Burling, I. R., and de Gouw, J.: Development and validation of a portable gas phase standard generation and calibration system for volatile organic compounds, *Atmospheric Measurement Techniques*, 3, 683-691, 10.5194/amt-3-683-2010, 2010.
- 35 Zhang, X., Cappa, C. D., Jathar, S. H., McVay, R. C., Ensberg, J. J., Kleeman, M. J., and Seinfeld, J. H.: Influence of vapor wall loss in laboratory chambers on yields of secondary organic aerosol, *Proceedings of the National Academy of Sciences of the United States of America*, 111, 5802-5807, 2014.

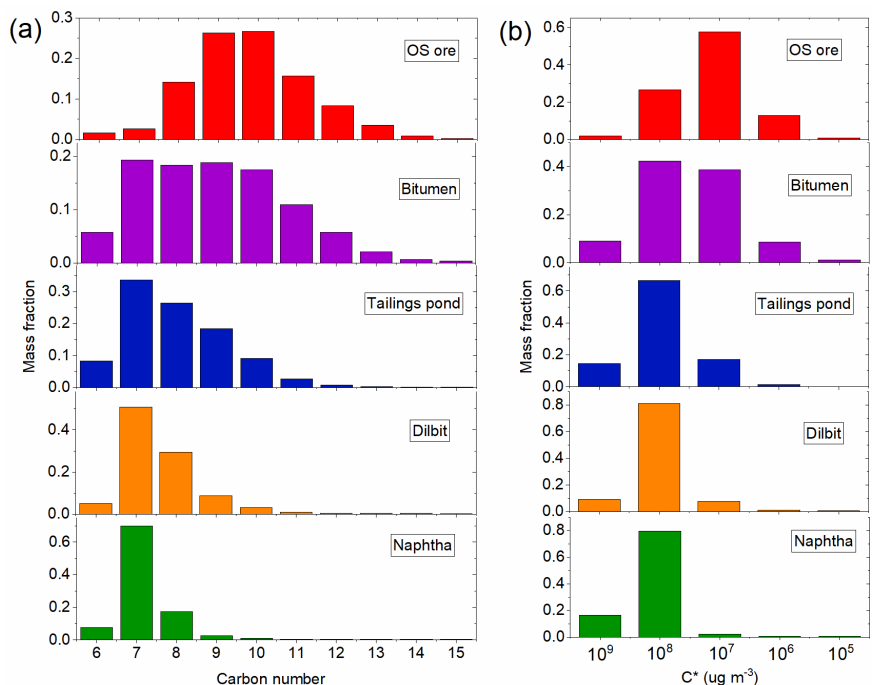


Figure 1. Volatility distribution of the OS-related precursors binned by carbon number (a) and effective saturation concentration C^* (b).

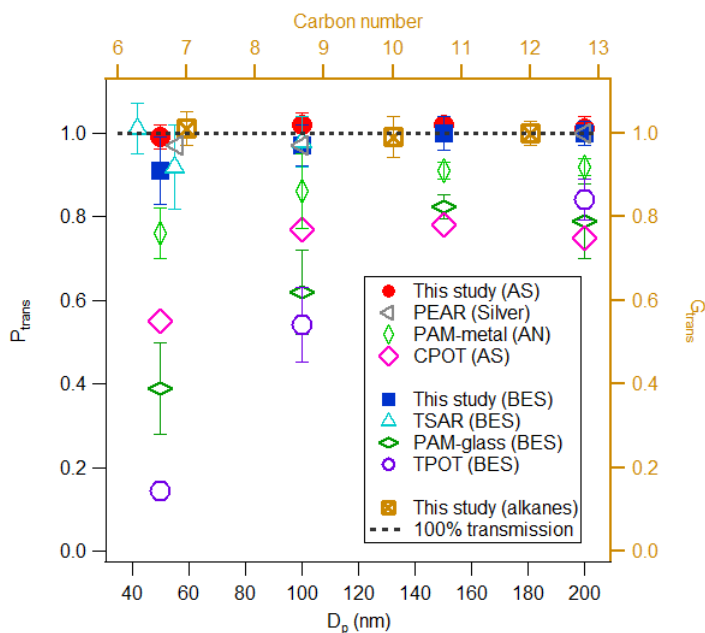


Figure 2. Particle (left and bottom axis) and gas (right and top axis) transmission efficiencies (P_{trans} and G_{trans}) for the ECCC-OFR. Particle transmission efficiencies of other OFRs are shown for comparison: PAM-glass and TPOT (Lambe et al., 2011), PAM-metal (Karjalainen et al., 2016), TSAR (Simonen et al., 2017), CPOT (Huang et al., 2017) and PEAR (Ihalainen et al., 2019).

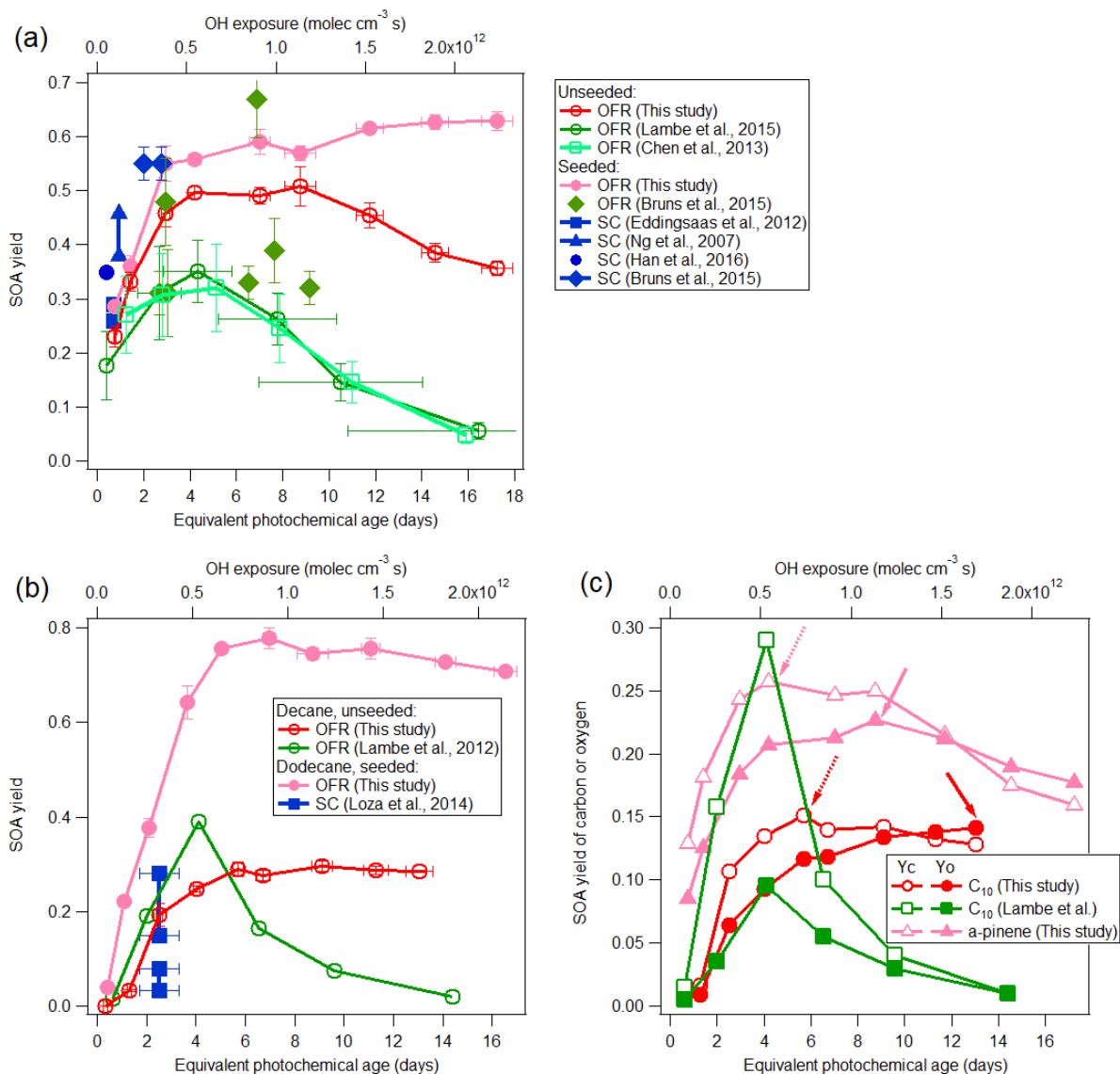


Figure 3. Low-NO_x SOA yields of α -pinene (a), *n*-decane (C₁₀) and *n*-dodecane (C₁₂) (b), compared to previous studies using OFRs and smog chambers (SCs) (Ng et al., 2007; Eddingsaas et al., 2012; Lambe et al., 2012; Chen et al., 2013; Loza et al., 2014; Lambe et al., 2015; Bruns et al., 2015; Han et al., 2016). The details regarding these comparisons are shown in Table 2. (c): SOA carbon and oxygen yields (Y_c and Y_o) for single precursors for unseeded experiments in the current study and in a previous study (Lambe et al., 2012). Dashed and solid arrows indicate the maximum of Y_c and Y_o, respectively.

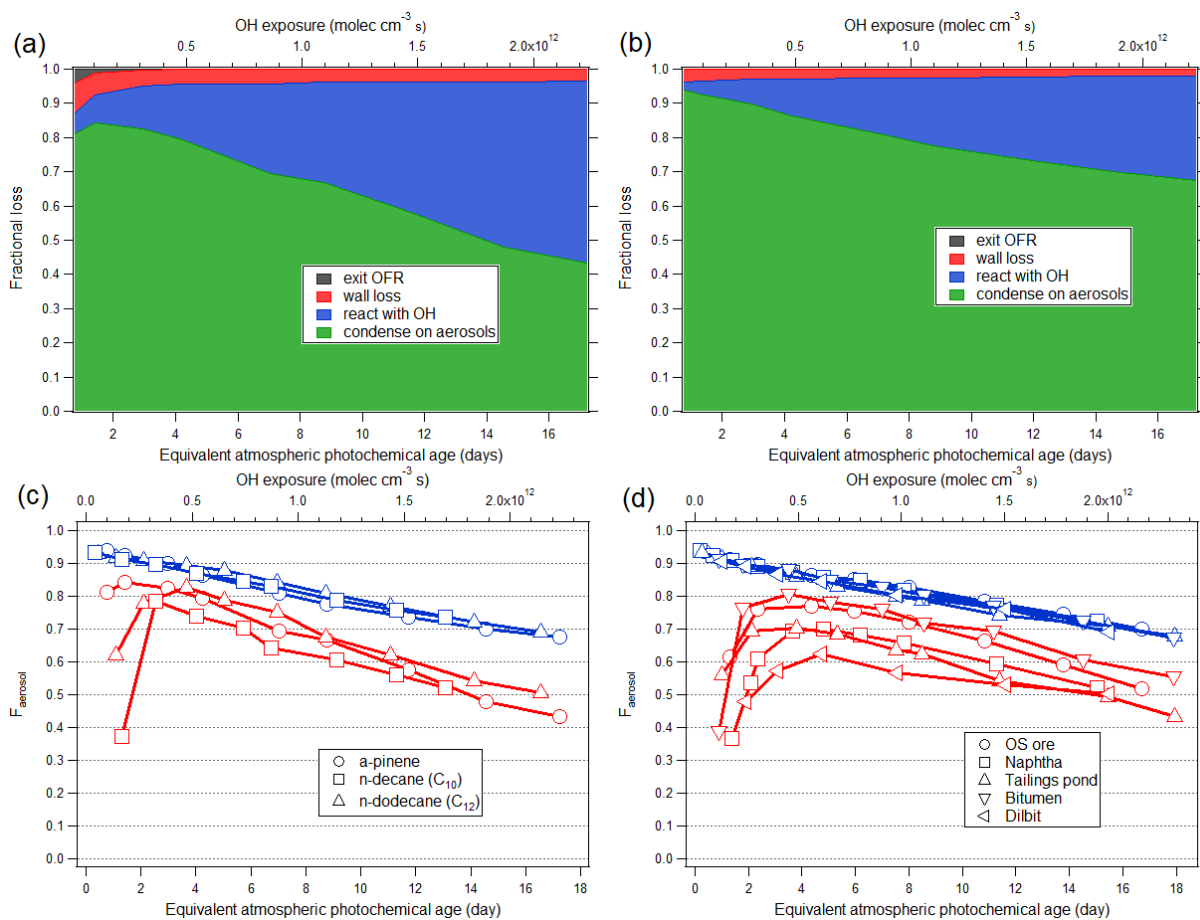


Figure 4. (a, b): The modeled fate of LVOCs in the current OFR as a function of photochemical age, for α -pinene oxidation, in the absence (a) and presence (b) of AS seed particles. (c, d): Fraction of LVOCs that condense on aerosol (F_{aerosol}) in the OFR during the oxidation of the single precursors (c) and various OS-related precursors (d) (blue: seeded experiments; red: unseeded experiments).

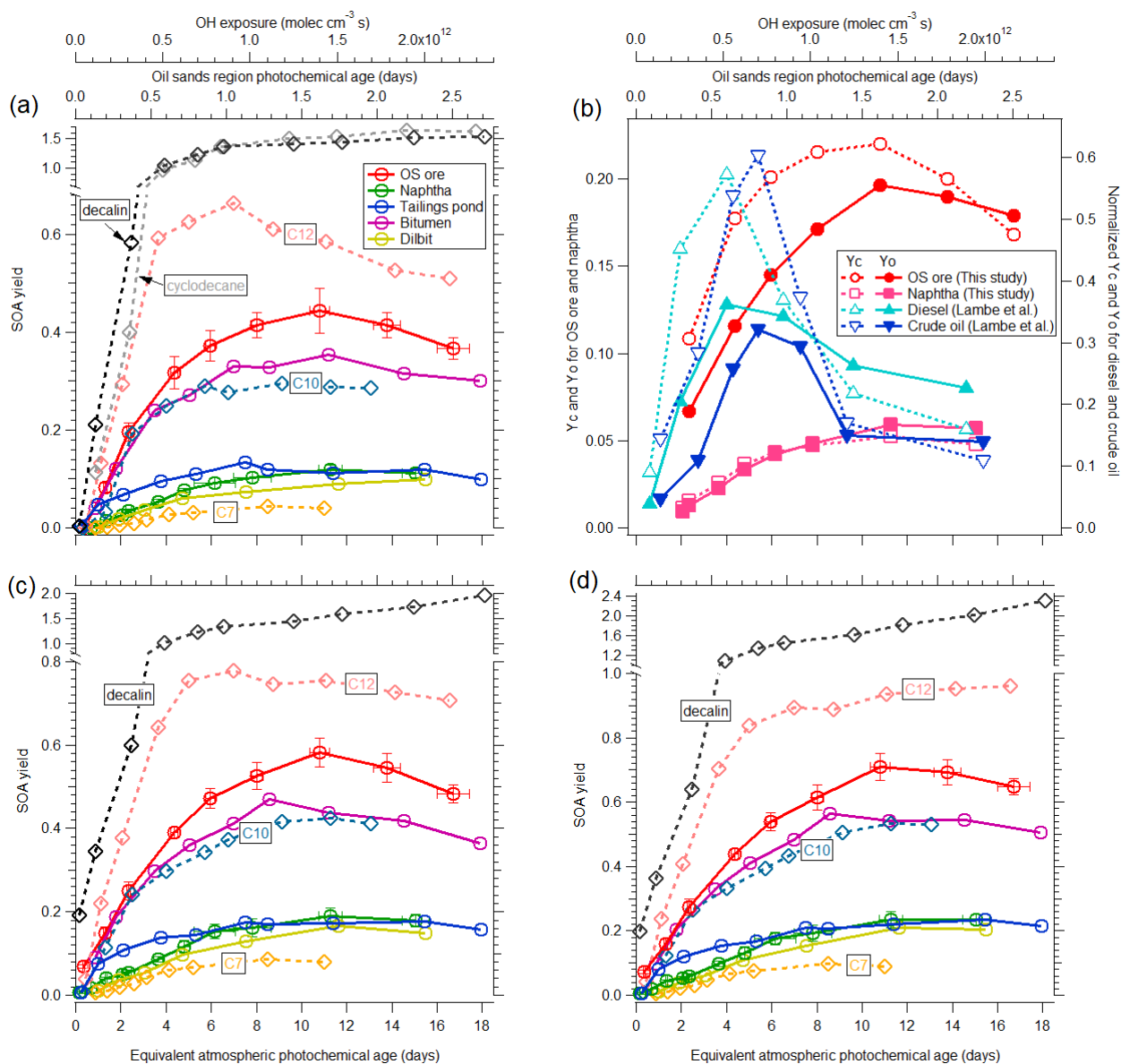


Figure 5. (a) SOA yields of OS-related precursors (OS ore, naphtha, tailings pond water, bitumen and dilbit) for unseeded experiments as a function of equivalent photochemical age and OH exposure. SOA yield of C₇, C₁₀ and C₁₂ *n*-alkanes, cyclodecane and decalin are also shown for comparison. Representative error bars indicate $\pm 1\sigma$ uncertainty in measurements. (b) SOA carbon and oxygen yields (Y_c and Y_o) for the OS precursors of lowest and highest volatility (OS ore and naphtha solvent) compared to normalized Y_c and Y_o for diesel and crude oil (Lambe et al., 2012). (c) SOA yields as in (a) in the presence of ammonium sulfate seed particles. (d) LVOCs fate corrected SOA yield of OS-related precursors and alkanes for seeded experiments. Note that the y-axis ranges are different in (a), (c), and (d).

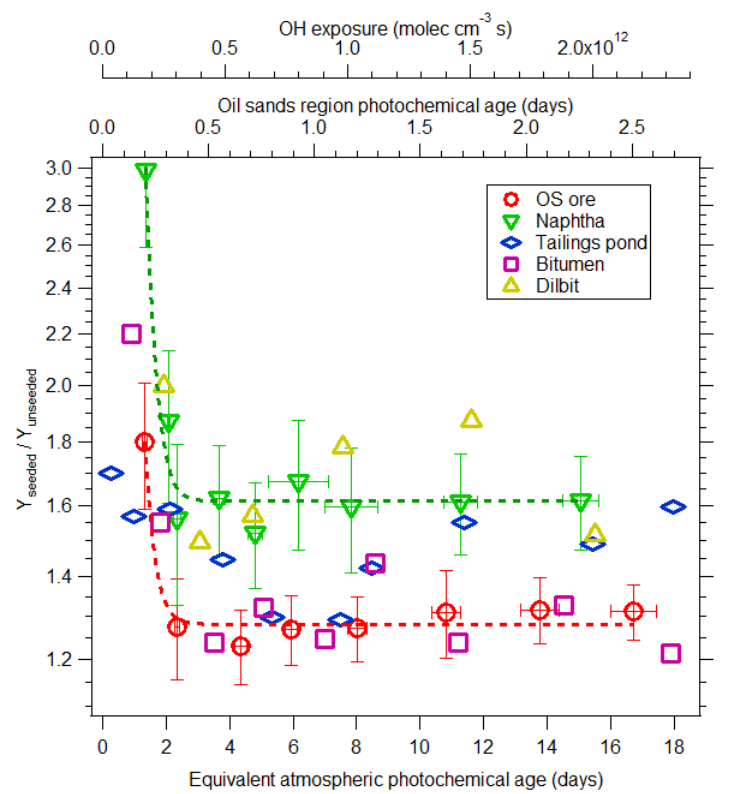


Figure 6. Yield enhancement factor due to seed particles for OS-related precursors. Dashed lines are exponential fittings for naphtha and OS ore data; error bars indicate $\pm 1\sigma$ uncertainty in measurements.

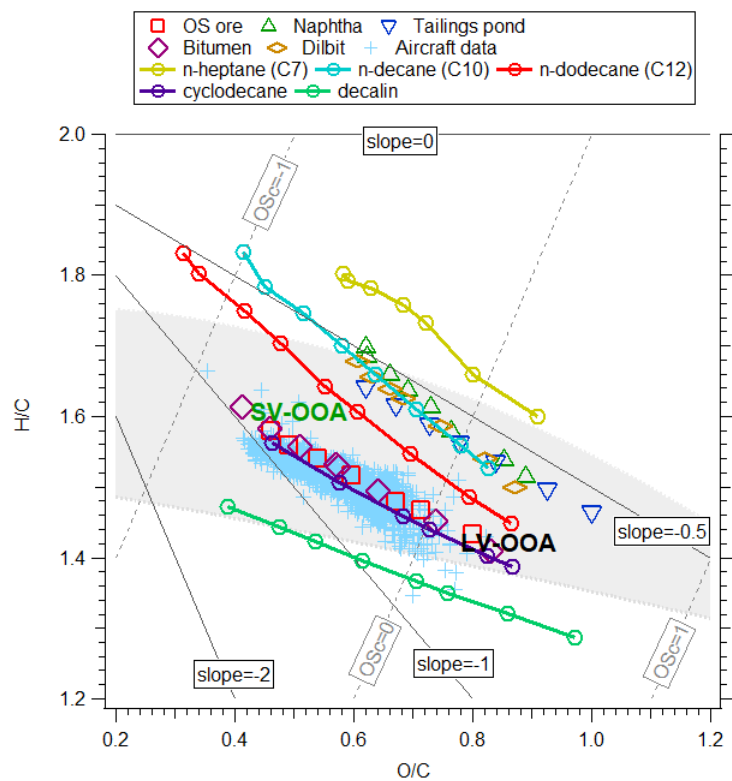


Figure 7. Van Krevelen diagram for the SOA formed from OS-related precursors, selected alkanes and recent aircraft data in oil sands plumes (Liggio et al., 2016). The shaded area represents the elemental ratio space associated with ambient OOA (Ng et al., 2011).

Table 1. Initial concentrations, maximum SOA mass concentrations and maximum yields of OS-related precursors and selected compounds.

Precursor name	Elemental formula	Initial carbon concentration (ppbC)		Maximum M _{SOA} (ug m ⁻³)		Maximum uncorrected yield ^a		Maximum corrected yield ^a	
		unseeded	seeded	unseeded	seeded	unseeded	seeded	unseeded	seeded
OS ore	-	137	137	35.4	46.3	0.444 (14)	0.581 (14)	0.644 (17.8)	0.708 (14)
Naphtha	-	674	677	46.7	75.1	0.118 (14.6)	0.191 (14.6)	0.193 (19.5) ^b	0.235 (14.6)
Tailings pond	-	291	288	22.7	29.8	0.134 (9.72)	0.176 (20)	0.216 (20)	0.279 (23.3) ^b
Bitumen	-	218	201	44.8	54.7	0.353 (14.5)	0.470 (11.1)	0.494 (23.2) ^b	0.545 (11.1)
Dilbit	-	710	710	41.0	69.2	0.099 (20.1) ^b	0.167 (15.1)	0.177 (20.1) ^b	0.209 (15.1)
<i>n</i> -Heptane	C ₇ H ₁₆	1675	1671	43.1	85.2	0.044 (11)	0.087 (11)	0.076 (11)	0.099 (11)
<i>n</i> -Decane	C ₁₀ H ₂₂	211.6	233.9	36.3	57.8	0.295 (11.8)	0.426 (14.6)	0.497 (16.9) ^b	0.534 (14.6)
<i>n</i> -Dodecane	C ₁₂ H ₂₆	109.8	114.7	42.2	51.7	0.663 (9)	0.778 (9)	0.906 (21.4) ^b	0.960 (21.4) ^b
Cyclodecane	C ₁₀ H ₂₀	60.3	-	56.6	-	1.639 (19)	-	2.121 (23) ^b	-
Decalin	C ₁₀ H ₁₈	50.5	50.5	43.7	55.7	1.532 (23.4) ^b	1.956 (23.4) ^b	2.004 (23.4) ^b	2.298 (23.4) ^b
α -Pinene	C ₁₀ H ₁₆	137	137	38.7	48.0	0.508 (11.4)	0.630 (22.3) ^b	0.731 (22.3) ^b	0.872 (22.3) ^b

a. The number shown in the brackets is the corresponding OH exposure (10¹¹ molecules cm⁻³ s).

5 b. The SOA yield does not reach a maximum over OH exposure range, as such the highest OH exposure is shown here.

Table 2. Comparison of experimental conditions and SOA yields with previous studies.

Precursor name	M _{seed} ($\mu\text{g m}^{-3}$)	[precursor] (ppb)	M _{SOA} ($\mu\text{g m}^{-3}$)	SOA yield	OH _{exp} ($10^{11} \text{ molec cm}^{-3} \text{ s}$)	Reactor ^c	Reference
<i>α</i> -pinene	0	41-100	-	0.35 ^a	5.57	OFR	Lambe et al. (2015)
	0	50.6	90	0.32 ^a	6.6	OFR	Chen et al. (2013)
	0	13.7	37.9	0.50 ^b	5.44	OFR	This study
	13-19	44.5-47.7	63.5-76.6	0.26-0.29	0.91	SC	Eddingsaas et al. (2012)
	14-21	13.8-47.5	29.3-121.3	0.38-0.46	1.21	SC	Ng et al. (2007)
	12.6	19.6	34.1	0.35	0.52	SC	Han et al. (2016)
	21	13.7	21.8	0.29 ^b	1	OFR	This study
	10-60	192-200	540-570	0.55-0.56	2.6-3.6	SC	Bruns et al. (2015)
	10-60	137-347	200-1000	0.31-0.67	3.5-11.9	OFR	Bruns et al. (2015)
21	13.7	41.9	0.55 ^b	3.9	OFR	This study	
<i>n</i> -decane	0	102	231	0.39 ^a	5.3	OFR	Lambe et al. (2012)
	0	23.4	30.4	0.25 ^b	5.2	OFR	This study
<i>n</i> -dodecane	17-24	8.2-34	1.8-65	0.03-0.28	3.24	SC	Loza et al. (2014)
	21	9.6	24.3	0.37 ^b	2.72	OFR	This study

a. Maximum SOA yield.

b. The SOA yield at the OH exposure similar to above studies.

5 c. OFR: oxidation flow reactor; SC: smog chamber.

Supplement of

Secondary organic aerosol formation from α -pinene, alkanes and oil sands related precursors in a new oxidation flow reactor

Kun Li, John Liggio, Patrick Lee, Chong Han, Qifan Liu, and Shao-Meng Li

Air Quality Research Division, Environment and Climate Change Canada, Toronto, Ontario M3H 5T4, Canada.

Correspondence: John Liggio (john.liggio@canada.ca)

S1. OFR comparisons

The design of the ECCC-OFR (Environment and Climate Change Canada oxidation flow reactor) was partially based upon recent OFRs designs (Lambe et al., 2011;Huang et al., 2017;Simonen et al., 2017) with several small specific differences. The specific differences and similarities between the various reported OFRs is described below.

Comparison with the PAM (Potential Aerosol Mass) reactor (Lambe et al., 2011):

The ECCC-OFR utilizes a conical diffusion inlet, while PAM employs a straight inlet. The straight inlet is likely to lead to some jetting and recirculation, while cone inlet should have improved fluid dynamics (Huang et al., 2017;Mitroo et al., 2018). The lamps of the ECCC-OFR are located on the outside of the reactor, while the lamps for the PAM are located inside the reactor which can increase surface-to-volume ratio and hence wall losses. Finally, both OFRs sample from the center with appropriate side flows as exhaust, however the ECCC-OFR uses a sampling tube which is 12.7 cm offset from the end of the OFR.

Comparison with CPOT (Caltech Photooxidation Flow Tube) (Huang et al., 2017):

Both of these OFRs use a conical diffusion inlet, with the lamps of both located out of the reactor. The full cone angle of CPOT (15°) is smaller than ECCC-OFR (30°). The ECCC-OFR samples from a center port, while CPOT samples all gases at the exit cone. The CPOT has a larger surface-to-volume ratio and a longer residence time (~1500 s) compared to the ECCC-OFR, which may lead to larger wall losses of particles and organic vapors.

Comparison with TSAR (TUT Secondary Aerosol Reactor) (Simonen et al., 2017):

Both of these OFRs make use of a conical inlet, with lamps located on the outside of the reactor. These OFRs both sample from the OFR center-line, with sampling tubes offset from the end of the reactors. The TSAR is designed for rapidly changing sources, with a volume that is smaller (3.3 L) and a residence time which is shorter (37 s) (Simonen et al., 2017). As a result, the OH concentration within the TSAR will be higher at the same OH exposure. The LVOCs inside the reactor can be consumed by high concentration of OH, or exit the OFR because due to insufficient time to condense on aerosols (Simonen et al., 2017).

Comparison with PEAR (Photochemical Emission Aging Flow Tube Reactor) (Ihalainen et al., 2019):

Both of these OFRs use a conical inlet, and they both sample from the center-line with appropriate side flows as exhaust. The full cone angle of PEAR (28°) is similar to ECCC-OFR (30°). The lamps of the ECCC-OFR are located on the outside of the reactor, while the lamps for the PEAR are located inside the reactor. The volume of PEAR (139 L) is larger than ECCC-OFR, and the flow rate is also larger, resulting in similar residence time.

S2. CFD simulations and RTD measurements

To assess the near laminar flow of the ECCC-OFR, computational fluid dynamics (CFD) simulations were performed using ANSYS Fluent software (Version 2019 R2) in three dimensions to characterize the flow field inside the ECCC-OFR. Hybrid tetrahedral-hexahedral mesh consisting of 5.7×10^5 computation cells were used.

Turbulence was modeled using a realizable k-epsilon model. The simulation results are shown in Fig. S4. It is shown in Fig. S4a that the flow velocity distribution in the reactor is generally uniform. A high velocity is observed only near the inlet, but reduces to the average velocity in the conical diffuser. The velocity distribution here indicates that jetting is much weaker in ECCC-OFR compared to PAM (Mitroo et al., 2018). Fig. S4b indicates that the flow field is quite good in ECCC-OFR, with a small recirculation zone, similar to previous studies using a conical diffusion inlet (Huang et al., 2017; Ihalainen et al., 2019), but much better than PAM (Mitroo et al., 2018).

The residence time distribution (RTD) was measured for ECCC-OFR and compared to ideal laminar flow in Fig. S5. The RTD was characterized by injecting a constant flow rate of CO₂ (10 s) into the OFR. The CO₂ concentration was then monitored from the sampling outlet of OFR with a CO₂ analyzer (Li-Cor LI-840A). The RTD was calculated from the differential CO₂ as a function of time elapsed since the start of injection. Fig. S5 indicates that the residence time associated with the CO₂ maximum intensity for the measured RTD and the ideal laminar flow RTD are in good agreement, and improved over the PAM and TPOT (Lambe et al., 2011). The shape of measured RTD before ~100 s is similar to the ideal laminar flow RTD, but slightly wider, which is likely due to dispersion. After ~100 s, the measured decrease in CO₂ is slower than for ideal laminar flow, which is likely due to recirculation in the OFR (Fig. S4).

S3. OS sample details

OS ore samples were collected directly from the CNRL-Horizon OPP (Ore Preparation Plant) surge bin #1 on 24-Sep-2016, and stored in a freezer (-10 °C). Once the oil sands is hauled out of the mine, the ore is first processed in an Ore Preparation Plant (OPP), where clumps of oil sands are broken down (OPP-dry) and mixed with water to produce a pumpable slurry (OPP-wet). Mined oil sands can contain large chunks of bitumen, ice and fine solids. The crusher and sizer of the OPP-dry process breaks these clumps down into a loose, unconsolidated material (OSM, 2019). The OS ore sample here is from the surge bin after the OPP-dry process, which can be considered as “unprocessed” OS ore.

Bitumen was collected from the bitumen froth from the CNRL-Horizon plant on 25-Sep-2016, and stored in a freezer (-10 °C). Bitumen froth is extracted from the oil sands slurry (after OPP-wet) through a simple water-based gravity separation process, which occurs in a large cone-bottomed vessel. The bitumen attaches to free air bubbles and rises to the top of the vessel, forming an intermediate froth product (the bitumen samples here) (OSM, 2019). The heavy sand sinks to the bottom and is pumped out to the tailings plant (OSM, 2019). Bitumen froth contains about 50-60% bitumen, 30-40% water and 10-15% fine solids.

Naphtha solvent was collected from the CNRL-Horizon facility on 25-Sep-2016, and stored in a refrigerator (~4 °C). Naphtha, a type of solvent/diluent used in the extraction and dilution of bitumen, is a mixture of C₃-C₁₄ hydrocarbons with major fractions of *n*-alkanes (e.g., heptanes, octane, nonane) and aromatics (e.g., benzene, toluene, ethylbenzene, xylenes) (Siddique et al., 2006).

Dilbit is diluted bitumen, and was collected from the CNRL-Horizon facility on 25-Sep-2016, and stored in a refrigerator ($\sim 4^\circ\text{C}$). Though bitumen froth contains only $\sim 60\%$ bitumen, it acts almost like a single-phase fluid. The water and bitumen are closely intermixed, with fine solids trapped within the viscous mixture (OSM, 2019). Therefore, bitumen froth is further processed by froth treatment, which is accomplished through the addition of a solvent or diluent (e.g., naphtha). This solvent/diluent dilutes the bitumen, producing a less viscous, lighter product, with a density lower than water. The viscosity of the diluted bitumen also drops significantly, which releases the trapped fines. The diluted bitumen floats to the top of the gravity separation vessel, leaving the fines to settle to the bottom of the water phase (OSM, 2019). Bitumen itself is extremely heavy and viscous, and cannot be transported in pipelines. The diluted bitumen also makes the transport in pipelines possible for bitumen products.

Tailings pond water was collected from Suncor pond 2/3 on 23-Aug-2017, and stored in a refrigerator ($\sim 4^\circ\text{C}$). Tailings are a mixture of water, fine silts, residual bitumen, salts and soluble organic compounds. They also include solvents (e.g., naphtha) that are added to the oil sands during the separation process. Suncor tailings pond 2/3 is considered as one of the most active tailings ponds in the Alberta OS region (Small et al., 2015).

S4. Volatility distribution of OS-related precursors

The total ion chromatogram of the OS-related precursors as a function of retention time for GC-MS are shown in Fig. S3. The retention time for *n*-alkane standards are also shown. Here we assume that the unresolved complex mixture between C_n to C_{n+1} alkanes have lower volatility than C_n and higher volatility than C_{n+1} , and bin the data (after response factor correction for compounds with different volatilities) by carbon number in Fig. 1a. According to the relationship between carbon number and volatility (Donahue et al., 2006), the data are also binned by effective saturation concentration (C^*) in Fig. 1b. For OS ore, the volatility covers a wide range of carbon number from 6 to 15. Based on the mass fraction of each carbon number, we calculated the average carbon number of OS ore, which is ~ 10 (9.79). As a commonly used solvent in OS processing, the naphtha has a narrow distribution mainly at $C_6 - C_8$, with a peak at C_7 . The VD of OS ore and bitumen are very similar at a retention time of > 4 min (Fig. S3), which corresponds to approximately C_8 , and indicates that the processed bitumen is essentially oil sands mixed with some solvents during the processing. Bitumen, dilbit and tailings pond water contain varying amounts of the similar solvents, consistent with the dominant volatility at C_7 for these samples. Based on the VDs in Fig. 1, the fraction of solvent within the emissions follows the order of naphtha (100% solvent) $>$ dilbit $>$ tailings pond $>$ bitumen $>$ OS ore (0% solvent). This corresponds to a non-solvent fraction in the sample vapors in the order of OS ore $>$ bitumen $>$ tailings pond $>$ dilbit $>$ naphtha (0% heavy oil). From the VDs in Fig. 1, it is also found that the vapors from OS ore and bitumen contain $\sim 15\%$ and $\sim 10\%$ IVOCs (carbon number ≥ 12 , $C^* \leq 10^6 \mu\text{g m}^{-3}$), respectively, while other precursors are almost 100% VOCs.

We note that VD of OS ore measured here is somewhat different from that previously measured (Liggio et al., 2016), which were mainly in the C_{12} to C_{16} range. However, the VD for OS ore in this study is mainly from C_8 to C_{13} with an average value of C_{10} , which are more volatile than the previous study. This difference is likely due to the nature

of the samples themselves, as the previous OS ore sample was collected off-site, in an area not associated with active mining, and exposed to the atmosphere for a long period. It is highly likely that the majority of the more volatile components had long since evaporated. Conversely, the current study utilized samples taken directly from the active mining operations (>50 m below ground) and immediately archived at -10 °C. In addition, the VD derived here are consistent with those from more recent aircraft measurements around active mining operations.

S5. Secondary particle yield calculations

The yield of sulfuric acid ($Y_{H_2SO_4}$) was calculated using the mass fraction of H_2SO_4 in particles ($x_{H_2SO_4}$), the SMPS-measured particle volume ($V_{H_2SO_4 \cdot H_2O}$, $nm^3 cm^{-3}$), the density of the particles ($\rho_{H_2SO_4 \cdot H_2O}$, $g cm^{-3}$), and the measurement of the reacted SO_2 (ΔSO_2 , ppb), using an approach which has been described in detail previously (Lambe et al., 2011):

$$Y_{H_2SO_4} = \frac{x_{H_2SO_4} \times V_{H_2SO_4 \cdot H_2O} \times \rho_{H_2SO_4 \cdot H_2O}}{3.95 \times \Delta SO_2}$$

The $x_{H_2SO_4}$ and $\rho_{H_2SO_4 \cdot H_2O}$ were estimated using the Extended Aerosol Inorganic Thermodynamic Model (E-AIM) I (<http://www.aim.env.uea.ac.uk/aim/aim.php>) (Carslaw et al., 1995). The dry yield of H_2SO_4 from OH oxidation of SO_2 is $3.95 \mu g m^{-3}$ per ppb SO_2 reacted (Lambe et al., 2011); hence $Y_{H_2SO_4}$ is expected to be 100% without wall losses.

The SOA yields (Y) are calculated using the mass concentration of organic aerosols (ΔM_O) and reacted parent hydrocarbons (ΔHC):

$$Y = \Delta M_O / \Delta HC$$

Here, ΔM_O is calculated by multiplying the integrated volume concentration by the effective particle density (see Methods). The calculation for ΔHC is based on the measured THC. From the measured total carbon (converted CO_2) mixing ratio, one can derive the carbon mass concentration [C]. For single precursors (which contains only C and H), the precursor mass concentration [HC] is calculated by:

$$[HC] = [C] \times \left(1 + \frac{H/C}{12}\right)$$

The reacted hydrocarbon mass concentration is then calculated by:

$$\Delta HC = [HC] \times (1 - e^{(-k \cdot [OH] \cdot t)})$$

where k is the second-order rate constant of the precursor with OH; $[OH] \cdot t$ is the OH exposure, which is measured off-line via the decay of CO (see Methods).

For OS-related precursors, the molecular composition (and hence H/C and k) is unknown, hence there are several assumptions when applying the above steps. The H/C of the OS precursors (H/C_{OS}) is estimated via the intercept of the linear fit of the Van Krevelen diagram of OS SOA (Fig. S10, Table S1). The intercept represents the H/C ratio

when O/C ratio is zero, which is expected to be similar to the precursor H/C. However, based on the intercept and the precursor H/C of the alkanes (Table S1), we find that the intercept generally underestimates the precursor H/C, with a correlation of $H/C = 0.606 + 0.768 \times \text{Intercept}$ ($R^2 = 0.97$). The H/C_{OS} are then calculated based on this equation, and are shown in Table S1. The uncertainty of this approach is estimated to be within ± 0.1 , which corresponds to minor uncertainty (less than 1%) in the calculated mass of OS precursors.

Based on the VDs of OS precursors as a function of carbon number (Fig. 1a), the reacted OS precursor mass concentration is estimated by two approaches. First, using the rate constants of the *n*-alkanes ($C_6 - C_{15}$) to calculate the reacted precursor in each bin, and adding them together to obtain the total reacted mass concentration. Second, using the rate constant of the *n*-alkane similar to the average carbon number (e.g., C_{10} for OS ore, see Sect. S4) as the rate constant of the OS precursor and calculating the reacted mass concentration. Figure S7 shows the calculated yields using these two approaches for OS ore. These two approaches give very similar yields, with both of them higher than the SOA potential (assuming all precursor reacted) at photochemical age of < 3 days. After 3 days, all of the curves are identical since the precursors are 100% reacted. In addition, we also calculate the yields assuming the OS ore has a rate constant of cyclodecane, with calculated yields slightly lower than assuming it to be *n*-decane. For other OS-related precursors, the results are similar to OS ore. As these approaches give very similar results and the average carbon method is simpler to conduct, the SOA yields of OS precursors shown in this study are all calculated based on the average carbon method using the rate constant of corresponding *n*-alkanes.

The carbon and oxygen yields (Y_C and Y_O) are also shown in this study, which are calculated by the method described previously (Kroll et al., 2009; Lambe et al., 2012):

$$Y_C = Y \times \frac{12}{12 + 16 \times O/C + H/C}$$

$$Y_O = \frac{Y_C \times O/C \times 16}{12}$$

S6. LVOCs fate correction

The fate of the LVOCs in the OFR include condensation on the reactor wall, exiting the reactor, and reacting with OH to form higher volatility compounds that are not condensable. These three losses may influence the LVOC fate, which in the atmosphere is expected to be condensation to pre-existing aerosol. Here, the method developed by Palm et al. (2016) was used to correct for these losses. Briefly, the lifetimes of LVOCs associated with these processes were used to estimate the fractional loss of each process. These lifetimes are τ_{aerosol} (condense on aerosol), τ_{wall} (condense on reactor wall), and τ_{OH} (react with OH to form non-condensable compounds) and their parametrization is described below:

1. τ_{aerosol} is estimated by (Pirjola et al., 1999):

$$\tau_{\text{aerosol}} = 1/(4\pi \cdot CS \cdot D)$$

where D is the diffusion coefficient, which is estimated to be $7 \times 10^{-6} \text{ m}^2 \text{ s}^{-1}$ for oxidized organic vapor with a molecular weight of 200 g mol^{-1} (Tang et al., 2015); CS is the “condensational sink”, which represents the sink associated with aerosols and is related to particle size distribution:

$$CS = \sum_i r_i \beta_i N_i$$

where r_i and N_i are the particle radius and number concentration of each size bin of SMPS. The β term is the correction factor for gaseous diffusion to the particle surface:

$$\beta = \frac{Kn + 1}{0.377Kn + 1 + \frac{4}{3}\alpha^{-1}Kn^2 + \frac{4}{3}\alpha^{-1}Kn}$$

where α is the mass accommodation coefficient (also known as the sticking coefficient) of condensing vapor, which is assumed to be 1; Kn is the Knudsen number:

$$Kn = 3 \sqrt{\frac{\pi M}{8RT}} \frac{D}{r}$$

where M is the molecular weight of the condensing vapor, which is assumed to be 200 g mol^{-1} ; R is the gas constant; T is the temperature.

2. τ_{wall} is estimated by (McMurry and Grosjean, 1985):

$$\tau_{wall} = \frac{\pi}{2 \frac{A}{V} \sqrt{k_e D}}$$

where A/V is the surface-area-to-volume ratio, which is 22.3 m^{-1} for our OFR; k_e is the eddy diffusion coefficient (Krechmer et al., 2016):

$$k_e = 0.004 + 0.0056 \cdot V^{0.74}$$

3. It is assumed that after reacting five times with OH, the LVOCs are fragmented to small molecules that are too volatile to condense (Palm et al., 2016). Hence, τ_{OH} is estimated by:

$$\tau_{OH} = \frac{5}{k_{OH} \cdot [OH]}$$

where k_{OH} is the rate constant for reaction with OH, which is assumed to be $1 \times 10^{-11} \text{ cm}^3 \text{ molec}^{-1} \text{ s}^{-1}$ (Ziemann and Atkinson, 2012).

Using the three lifetimes above, the total lifetime of these three pathways (τ_{total}) can be estimated by:

$$\frac{1}{\tau_{total}} = \frac{1}{\tau_{aerosol}} + \frac{1}{\tau_{wall}} + \frac{1}{\tau_{OH}}$$

Combined with the residence time (τ_{OFR}), the fraction that exit the OFR (F_{exit}), condense on aerosol ($F_{aerosol}$), condense on reactor wall (F_{wall}), and react with OH (F_{OH}) can be estimated using the following equations:

$$F_{exit} = e^{-\frac{\tau_{OFR}}{\tau_{total}}}$$

$$F_{aerosol} = (1 - F_{exit}) \cdot \frac{\tau_{total}}{\tau_{aerosol}}$$

$$F_{wall} = (1 - F_{exit}) \cdot \frac{\tau_{total}}{\tau_{wall}}$$

$$F_{OH} = (1 - F_{exit}) \cdot \frac{\tau_{total}}{\tau_{OH}}$$

According to the sensitivity analysis performed previously (Palm et al., 2016), variations in most of parameters above have little influence on the results with the exception of CS and α . The CS that used in this method is the average value at the beginning and the end of the reactor. Using a CS at the beginning of the reactor will largely enhance the correction factor. However, as organic aerosols are formed through the entire reactor, using the average CS is more reasonable. Varying α from 1 to 0.1 also largely enhances the correction factor. However, according to a recent study (Krechmer et al., 2017), the accommodation coefficient was quantified to be ~ 1 . Hence the influence from α is likely to be small. Overall, we assume that the uncertainty associated with this correction approach is within $\pm 30\%$.

When applying the above correction to SOA yields, one needs to know the LVOCs fraction in SOA. The LVOCs and ELVOCs (extremely low volatility VOCs) in the atmosphere are $\sim 100\%$ in the particle phase, while the S/IVOCs may be partially in the gas phase, depending on the organic aerosol concentration. As a result, a OFR fate correction for S/IVOCs is not feasible. Previous field measurements and laboratory studies demonstrated that SOA from various sources were mainly $\sim 40\%$ - 80% L/ELVOCs and $\sim 20\%$ - 60% S/IVOCs (Hong et al., 2017; Saha et al., 2017; D'Ambro et al., 2018; Sato et al., 2018; Saha et al., 2018). In our experiments, the low- NO_x yields are significantly higher than the high- NO_x yields (paper in preparation), indicating a lower volatility for SOA formed under low- NO_x conditions. Hence, the upper limit of the fraction (80%) is used for the LVOCs correction of low- NO_x yields. The 20% S/IVOCs in SOA remain unchanged. Previous studies have assumed SOA to be 100% LVOCs (Ortega et al., 2016; Palm et al., 2016), and the 80% LVOCs used here leads to slightly lower correction factors.

S7. Conversion efficiency determination of the THC system

The conversion efficiency of the catalyst in the THC system is determined by injecting a small constant volume of liquid hydrocarbon into a constant flow of zero air using a syringe pump (Harvard apparatus 11A Plus). In our measurement, the liquid flow rate was 0.005 - $0.1 \mu\text{L min}^{-1}$ depending on the volatility, and the flow rate of zero air was 5 - 10 L min^{-1} . The airflow was at room temperature for high volatility compounds (e.g., toluene), while it is maintained at 60 - $100 \text{ }^\circ\text{C}$ for low volatility compounds (e.g., octadecane) to ensure that the hydrocarbon was 100% evaporated. The mixing ratio of the hydrocarbon was then calculated by:

$$HC(ppb) = \frac{RT\rho F_l \times 10^9}{MPF_g}$$

where R is the gas constant; T is the temperature; ρ is the density of the liquid; F_l is the flow rate of the liquid; M is the molecular weight; P is the atmospheric pressure; F_g is the zero air flow rate.

Figures and Tables

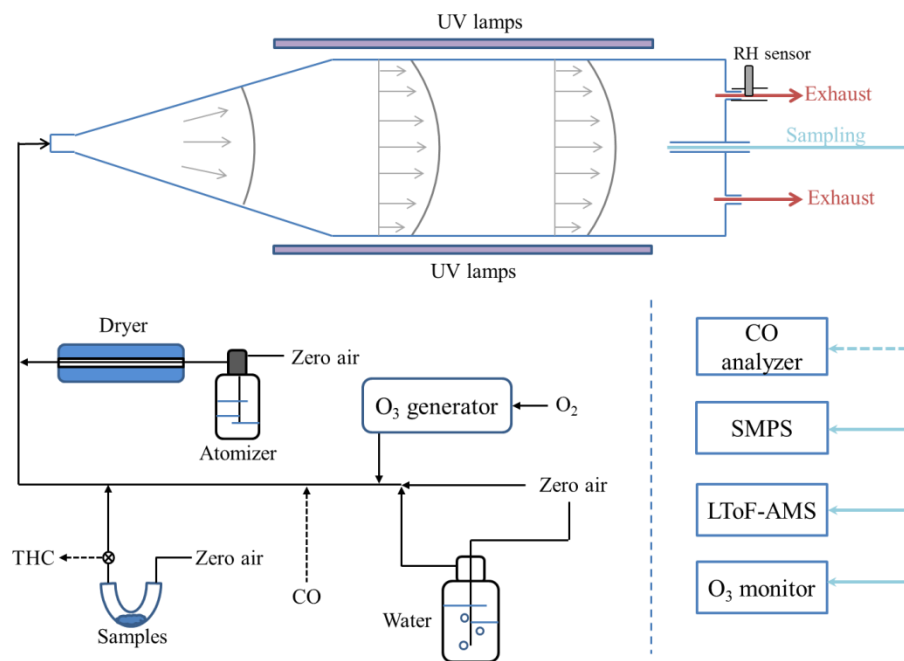


Figure S1. Schematic diagram of the ECCC-OFR and associated experimental setup.

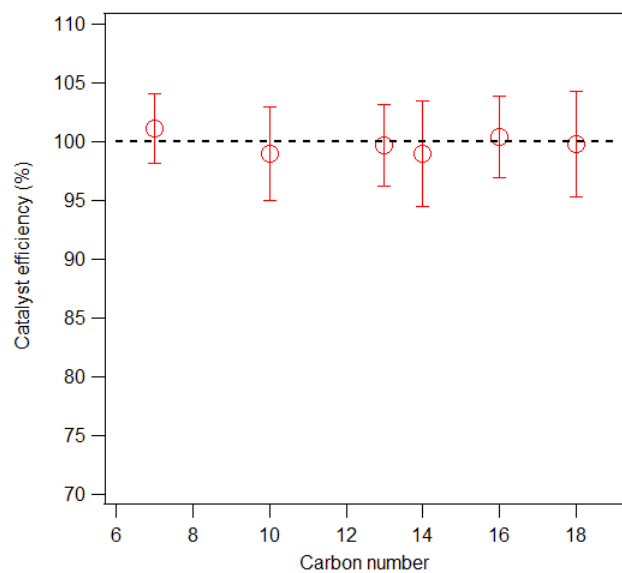


Figure S2. Catalyst efficiencies of the THC system for toluene and C₁₀, C₁₃, C₁₄, C₁₆, and C₁₈ *n*-alkanes.

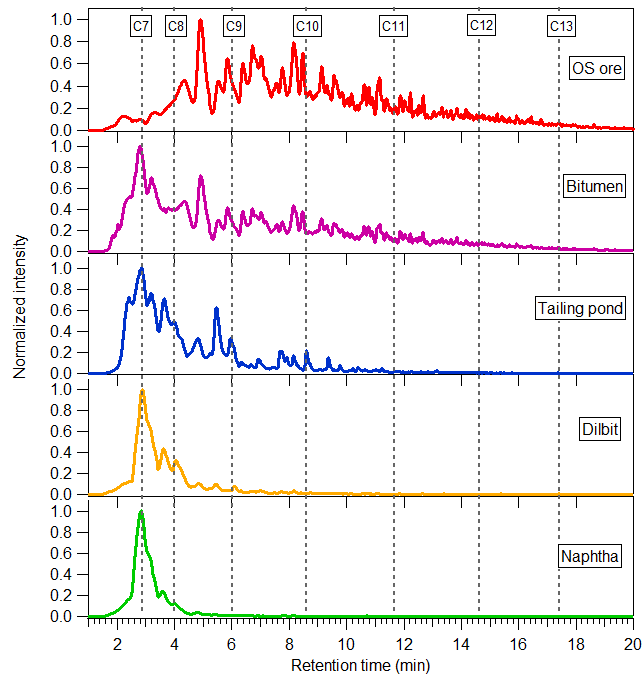


Figure S3. GC-MS chromatogram of the OS-related precursors. Dashed lines indicate the retention time of the *n*-alkanes from C₇ to C₁₃.

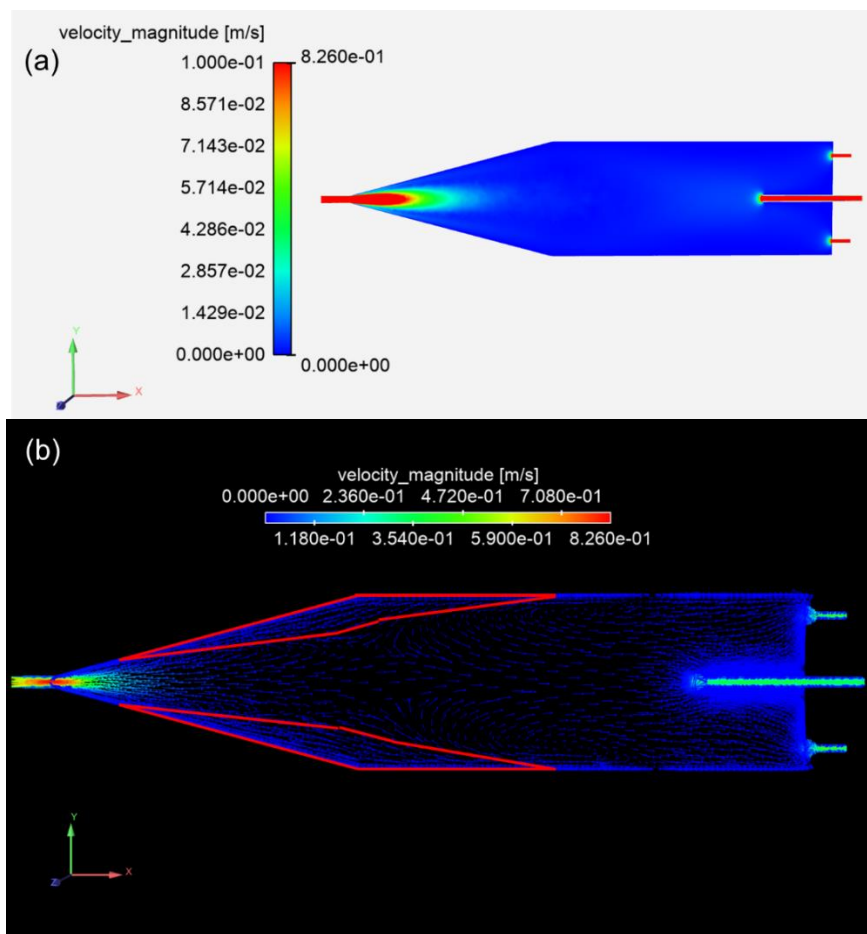


Figure S4. CFD simulation results: (a) velocity distribution; (b) vectors showing flow field. The red lines in (b) indicate the areas with recirculation.

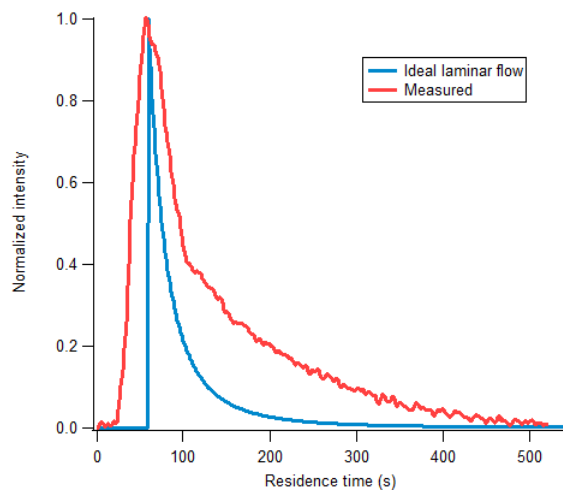


Figure S5. Residence time distribution (RTD) of CO₂ in ECCC-OFR compared to ideal laminar flow.

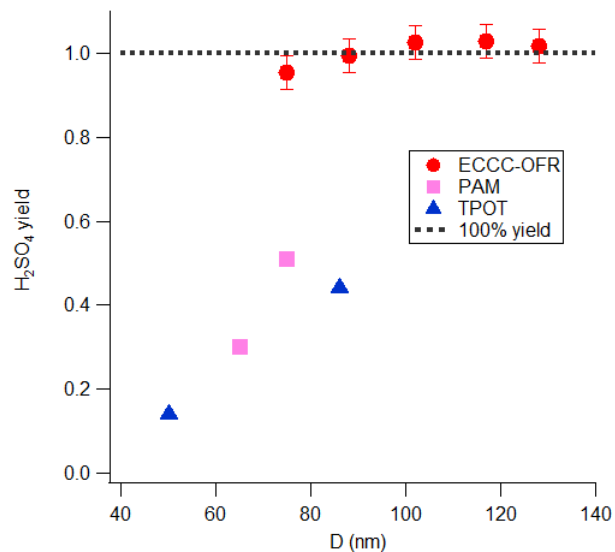


Figure S6. H₂SO₄ yields as a function of particle diameter in the ECCC-OFR and previous OFRs (Lambe et al., 2011).

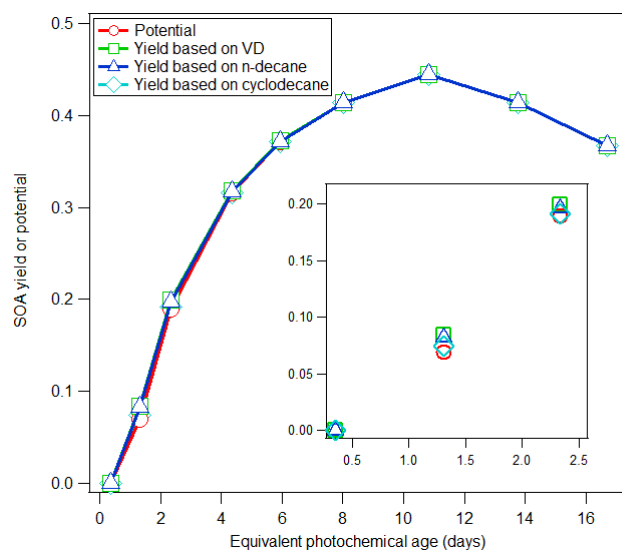


Figure S7. OS ore SOA potential and yield based on the reaction rate constant from the VD, *n*-decane and cyclodecane. The inset shows the first three photochemical ages.

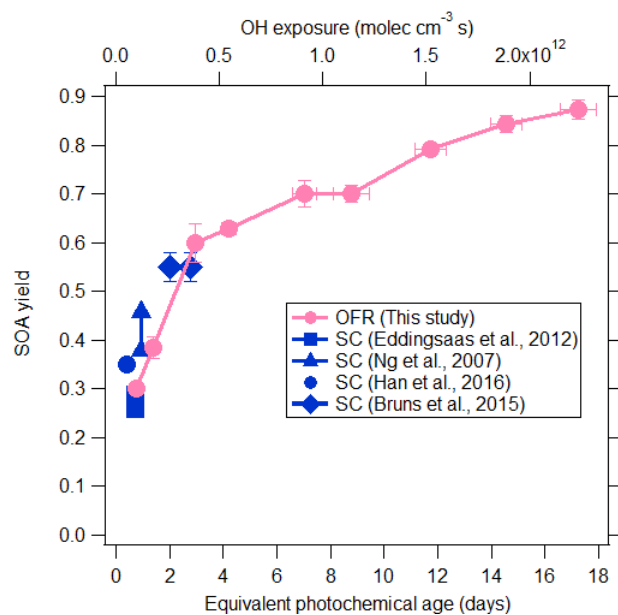


Figure S8. Comparison of LVOCs fate corrected SOA yields for α -pinene with previous smog chamber studies (Ng et al., 2007; Eddingsaas et al., 2012; Bruns et al., 2015; Han et al., 2016).

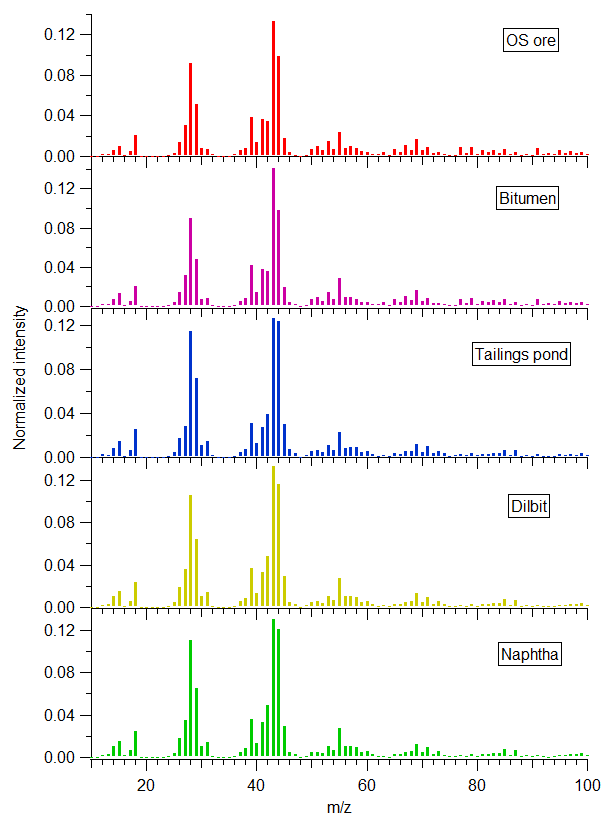


Figure S9. Representative AMS mass spectra for each OS-related oxidation experiment at OH exposure of $\sim 1.5 \times 10^{12}$ molec cm^{-3} s.

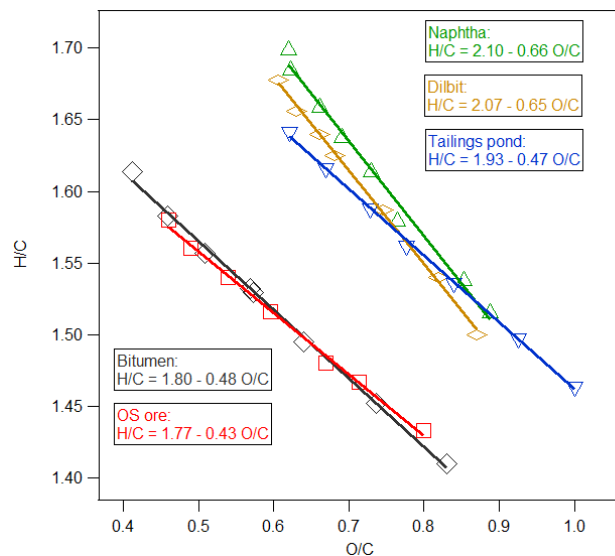


Figure S10. Linear regression of the H/C versus O/C ratios of SOA formed from OS-related precursors.

Table S1. Intercept and slope of the linear regression of the H/C versus O/C ratios in Fig. 7, and the H/C ratio of the precursors.

Precursor	Intercept	Slope	R ²	Precursor H/C
<i>n</i> -Heptane (C7)	2.17	-0.63	0.983	2.29
<i>n</i> -Decane (C10)	2.12	-0.72	0.996	2.2
<i>n</i> -Dodecane (C12)	2.04	-0.70	0.996	2.17
Cyclodecane	1.76	-0.43	0.995	2
Decalin	1.59	-0.32	0.999	1.8
Naphtha	2.10	-0.66	0.989	2.22 ^a
Dilbit	2.07	-0.65	0.998	2.2 ^a
Tailings pond	1.93	-0.47	0.999	2.09 ^a
Bitumen	1.80	-0.48	0.997	1.99 ^a
OS ore	1.77	-0.43	0.996	1.96 ^a

a. Calculated based on the linear fitting result of precursor H/C and intercept for alkanes (see Sect. S5).

References

Bruns, E. A., El Haddad, I., Keller, A., Klein, F., Kumar, N. K., Pieber, S. M., Corbin, J. C., Slowik, J. G., Brune, W. H., Baltensperger, U., and Prévôt, A. S. H.: Inter-comparison of laboratory smog chamber and flow reactor systems on organic aerosol yield and composition, *Atmospheric Measurement Techniques*, 8, 2315-2332, 10.5194/amt-8-2315-2015, 2015.

- Carslaw, K. S., Clegg, S. L., and Brimblecombe, P.: A Thermodynamic Model of the System HCl-HNO₃-H₂SO₄-H₂O, Including Solubilities of HBr, from <200 to 328 K, *The Journal of Physical Chemistry*, 99, 11557-11574, 10.1021/j100029a039, 1995.
- D'Ambro, E. L., Schobesberger, S., Zaveri, R. A., Shilling, J. E., Lee, B. H., Lopez-Hilfiker, F. D., Mohr, C., and Thornton, J. A.: Isothermal Evaporation of α -Pinene Ozonolysis SOA: Volatility, Phase State, and Oligomeric Composition, *ACS Earth and Space Chemistry*, 2, 1058-1067, 10.1021/acsearthspacechem.8b00084, 2018.
- Donahue, N. M., Robinson, A. L., Stanier, C. O., and Pandis, S. N.: Coupled partitioning, dilution, and chemical aging of semivolatile organics, *Environmental science & technology*, 40, 2635-2643, 10.1021/es052297c, 2006.
- Eddingsaas, N. C., Loza, C. L., Yee, L. D., Chan, M., Schilling, K. A., Chhabra, P. S., Seinfeld, J. H., and Wennberg, P. O.: α -pinene photooxidation under controlled chemical conditions – Part 2: SOA yield and composition in low- and high-NO_x environments, *Atmospheric Chemistry and Physics*, 12, 7413-7427, 10.5194/acp-12-7413-2012, 2012.
- Han, Y., Stroud, C. A., Liggi, J., and Li, S.-M.: The effect of particle acidity on secondary organic aerosol formation from α -pinene photooxidation under atmospherically relevant conditions, *Atmospheric Chemistry and Physics*, 16, 13929-13944, 10.5194/acp-16-13929-2016, 2016.
- Hong, J., Äijälä, M., Häme, S. A. K., Hao, L., Duplissy, J., Heikkinen, L. M., Nie, W., Mikkilä, J., Kulmala, M., Prisle, N. L., Virtanen, A., Ehn, M., Paasonen, P., Worsnop, D. R., Riipinen, I., Petäjä, T., and Kerminen, V.-M.: Estimates of the organic aerosol volatility in a boreal forest using two independent methods, *Atmospheric Chemistry and Physics*, 17, 4387-4399, 10.5194/acp-17-4387-2017, 2017.
- Huang, Y., Coggon, M. M., Zhao, R., Lignell, H., Bauer, M. U., Flagan, R. C., and Seinfeld, J. H.: The Caltech Photooxidation Flow Tube reactor: design, fluid dynamics and characterization, *Atmospheric Measurement Techniques*, 10, 839-867, 10.5194/amt-10-839-2017, 2017.
- Ihalainen, M., Tiitta, P., Czech, H., Yli-Pirilä, P., Hartikainen, A., Kortelainen, M., Tissari, J., Stengel, B., Sklorz, M., Suhonen, H., Lamberg, H., Leskinen, A., Kiendler-Scharr, A., Harndorf, H., Zimmermann, R., Jokiniemi, J., and Sippula, O.: A novel high-volume Photochemical Emission Aging flow tube Reactor (PEAR), *Aerosol Science and Technology*, 53, 276-294, 10.1080/02786826.2018.1559918, 2019.
- Krechmer, J. E., Pagonis, D., Ziemann, P. J., and Jimenez, J. L.: Quantification of Gas-Wall Partitioning in Teflon Environmental Chambers Using Rapid Bursts of Low-Volatility Oxidized Species Generated in Situ, *Environmental science & technology*, 50, 5757-5765, 10.1021/acs.est.6b00606, 2016.
- Krechmer, J. E., Day, D. A., Ziemann, P. J., and Jimenez, J. L.: Direct Measurements of Gas/Particle Partitioning and Mass Accommodation Coefficients in Environmental Chambers, *Environmental science & technology*, 51, 11867-11875, 10.1021/acs.est.7b02144, 2017.
- Kroll, J. H., Smith, J. D., Che, D. L., Kessler, S. H., Worsnop, D. R., and Wilson, K. R.: Measurement of fragmentation and functionalization pathways in the heterogeneous oxidation of oxidized organic aerosol, *Physical Chemistry Chemical Physics*, 11, 8005-8014, 10.1039/b905289e, 2009.
- Lambe, A. T., Ahern, A. T., Williams, L. R., Slowik, J. G., Wong, J. P. S., Abbatt, J. P. D., Brune, W. H., Ng, N. L., Wright, J. P., Croasdale, D. R., Worsnop, D. R., Davidovits, P., and Onasch, T. B.: Characterization of aerosol photooxidation flow reactors: heterogeneous oxidation, secondary organic aerosol formation and cloud condensation nuclei activity measurements, *Atmospheric Measurement Techniques*, 4, 445-461, 10.5194/amt-4-445-2011, 2011.
- Lambe, A. T., Onasch, T. B., Croasdale, D. R., Wright, J. P., Martin, A. T., Franklin, J. P., Massoli, P., Kroll, J. H., Canagaratna, M. R., Brune, W. H., Worsnop, D. R., and Davidovits, P.: Transitions from functionalization to fragmentation reactions of laboratory secondary organic aerosol (SOA) generated from the OH oxidation of alkane precursors, *Environmental science & technology*, 46, 5430-5437, 10.1021/es300274t, 2012.
- Liggi, J., Li, S. M., Hayden, K., Taha, Y. M., Stroud, C., Darlington, A., Drollette, B. D., Gordon, M., Lee, P., Liu, P., Leithead, A., Moussa, S. G., Wang, D., O'Brien, J., Mittermeier, R. L., Brook, J. R., Lu, G., Staebler, R. M., Han, Y., Tokarek, T. W., Osthoff, H. D., Makar, P. A., Zhang, J., Plata, D. L., and Gentner, D. R.: Oil sands operations as a large source of secondary organic aerosols, *Nature*, 534, 91-94, 10.1038/nature17646, 2016.
- McMurry, P. H., and Grosjean, D.: GAS AND AEROSOL WALL LOSSES IN TEFLON FILM SMOG CHAMBERS, *Environmental science & technology*, 19, 1176-1182, 10.1021/es00142a006, 1985.
- Mitroo, D., Sun, Y., Combet, D. P., Kumar, P., and Williams, B. J.: Assessing the degree of plug flow in oxidation flow reactors (OFRs): a study on a potential aerosol mass (PAM) reactor, *Atmospheric Measurement Techniques*, 11, 1741-1756, 10.5194/amt-11-1741-2018, 2018.

- Ng, N. L., Chhabra, P. S., Chan, A. W. H., Surratt, J. D., Kroll, J. H., Kwan, A. J., McCabe, D. C., Wennberg, P. O., Sorooshian, A., Murphy, S. M., Dalleska, N. F., Flagan, R. C., and Seinfeld, J. H.: Effect of NO(x) level on secondary organic aerosol (SOA) formation from the photooxidation of terpenes, *Atmospheric Chemistry and Physics*, 7, 5159-5174, 2007.
- Ortega, A. M., Hayes, P. L., Peng, Z., Palm, B. B., Hu, W., Day, D. A., Li, R., Cubison, M. J., Brune, W. H., Graus, M., Warneke, C., Gilman, J. B., Kuster, W. C., de Gouw, J., Gutiérrez-Montes, C., and Jimenez, J. L.: Real-time measurements of secondary organic aerosol formation and aging from ambient air in an oxidation flow reactor in the Los Angeles area, *Atmospheric Chemistry and Physics*, 16, 7411-7433, 10.5194/acp-16-7411-2016, 2016.
- OSM: Oil Sands Magazine, Technical Guides, <https://www.oilsandsmagazine.com/technical/> (last access: 13 February 2019), 2019.
- Palm, B. B., Campuzano-Jost, P., Ortega, A. M., Day, D. A., Kaser, L., Jud, W., Karl, T., Hansel, A., Hunter, J. F., Cross, E. S., Kroll, J. H., Peng, Z., Brune, W. H., and Jimenez, J. L.: In situ secondary organic aerosol formation from ambient pine forest air using an oxidation flow reactor, *Atmospheric Chemistry and Physics*, 16, 2943-2970, 10.5194/acp-16-2943-2016, 2016.
- Pirjola, L., Kulmala, M., Wilck, M., Bischoff, A., Stratmann, F., and Otto, E.: FORMATION OF SULPHURIC ACID AEROSOLS AND CLOUD CONDENSATION NUCLEI: AN EXPRESSION FOR SIGNIFICANT NUCLEATION AND MODEL COMPARISON, *Journal of Aerosol Science*, 30, 1079-1094, [https://doi.org/10.1016/S0021-8502\(98\)00776-9](https://doi.org/10.1016/S0021-8502(98)00776-9), 1999.
- Saha, P. K., Khlystov, A., Yahya, K., Zhang, Y., Xu, L., Ng, N. L., and Grieshop, A. P.: Quantifying the volatility of organic aerosol in the southeastern US, *Atmospheric Chemistry and Physics*, 17, 501-520, 10.5194/acp-17-501-2017, 2017.
- Saha, P. K., Khlystov, A., and Grieshop, A. P.: Downwind evolution of the volatility and mixing state of near-road aerosols near a US interstate highway, *Atmospheric Chemistry and Physics*, 18, 2139-2154, 10.5194/acp-18-2139-2018, 2018.
- Sato, K., Fujitani, Y., Inomata, S., Morino, Y., Tanabe, K., Ramasamy, S., Hikida, T., Shimono, A., Takami, A., Fushimi, A., Kondo, Y., Imamura, T., Tanimoto, H., and Sugata, S.: Studying volatility from composition, dilution, and heating measurements of secondary organic aerosols formed during α -pinene ozonolysis, *Atmospheric Chemistry and Physics*, 18, 5455-5466, 10.5194/acp-18-5455-2018, 2018.
- Siddique, T., Fedorak, P. M., and Foght, J. M.: Biodegradation of Short-Chain n-Alkanes in Oil Sands Tailings under Methanogenic Conditions, *Environmental science & technology*, 40, 5459-5464, 10.1021/es060993m, 2006.
- Simonen, P., Saukko, E., Karjalainen, P., Timonen, H., Bloss, M., Aakko-Saksa, P., Rönkkö, T., Keskinen, J., and Dal Maso, M.: A new oxidation flow reactor for measuring secondary aerosol formation of rapidly changing emission sources, *Atmospheric Measurement Techniques*, 10, 1519-1537, 10.5194/amt-10-1519-2017, 2017.
- Small, C. C., Cho, S., Hashisho, Z., and Ulrich, A. C.: Emissions from oil sands tailings ponds: Review of tailings pond parameters and emission estimates, *Journal of Petroleum Science and Engineering*, 127, 490-501, <https://doi.org/10.1016/j.petrol.2014.11.020>, 2015.
- Tang, M. J., Shiraiwa, M., Pöschl, U., Cox, R. A., and Kalberer, M.: Compilation and evaluation of gas phase diffusion coefficients of reactive trace gases in the atmosphere: Volume 2. Diffusivities of organic compounds, pressure-normalised mean free paths, and average Knudsen numbers for gas uptake calculations, *Atmospheric Chemistry and Physics*, 15, 5585-5598, 10.5194/acp-15-5585-2015, 2015.
- Ziemann, P. J., and Atkinson, R.: Kinetics, products, and mechanisms of secondary organic aerosol formation, *Chemical Society reviews*, 41, 6582-6605, 10.1039/c2cs35122f, 2012.